Sensors for shunts

Wearable sensors detect ventricular catheter shunt malfunction in patients with hydrocephalus

Krishnan et al./*Science Translational Medicine*

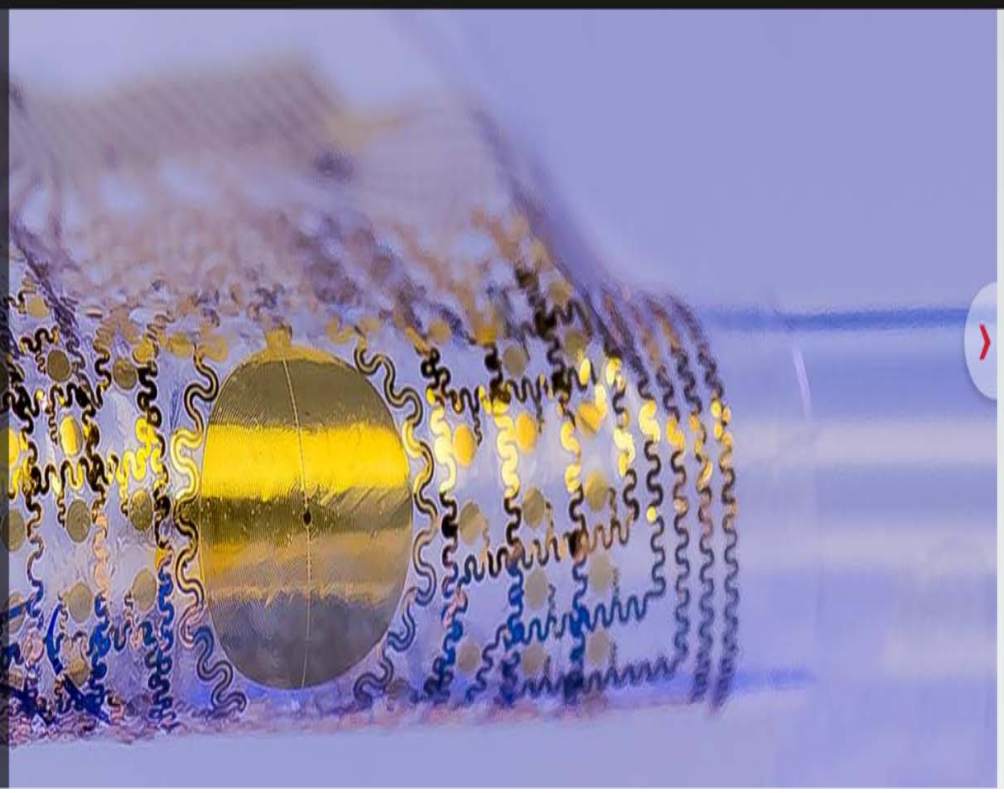

BIOSENSORS

Epidermal electronics for noninvasive, wireless, quantitative assessment of ventricular shunt function in patients with hydrocephalus

Siddharth R. Krishnan[1,2,3]*, Tyler R. Ray[2,3]*, Amit B. Ayer[4]*, Yinji Ma[5], Philipp Gutruf[2,3], KunHyuck Lee[2,3], Jong Yoon Lee[6], Chen Wei[7], Xue Feng[5], Barry Ng[1], Zachary A. Abecassis[8], Nikhil Murthy[4], Izabela Stankiewicz[9], Juliet Freudman[9], Julia Stillman[2], Natalie Kim[2], Grace Young[1], Camille Goudeseune[10], John Ciraldo[11], Matthew Tate[4], Yonggang Huang[2,7], Matthew Potts[4,12†], John A. Rogers[1,2,3,4,9†]

Hydrocephalus is a common and costly neurological condition caused by the overproduction and/or impaired resorption of cerebrospinal fluid (CSF). The current standard of care, ventricular catheters (shunts), is prone to failure, which can result in nonspecific symptoms such as headaches, dizziness, and nausea. Current diagnostic tools for shunt failure such as computed tomography (CT), magnetic resonance imaging (MRI), radionuclide shunt patency studies (RSPSs), and ice pack–mediated thermodilution have disadvantages including high cost, poor accuracy, inconvenience, and safety concerns. Here, we developed and tested a noninvasive, skin-mounted, wearable measurement platform that incorporates arrays of thermal sensors and actuators for precise, continuous, or intermittent measurements of flow through subdermal shunts, without the drawbacks of other methods. Systematic theoretical and experimental benchtop studies demonstrate high performance across a range of practical operating conditions. Advanced electronics designs serve as the basis of a wireless embodiment for continuous monitoring based on rechargeable batteries and data transmission using Bluetooth protocols. Clinical studies involving five patients validate the sensor's ability to detect the presence of CSF flow ($P = 0.012$) and further distinguish between baseline flow, diminished flow, and distal shunt failure. Last, we demonstrate processing algorithms to translate measured data into quantitative flow rate. The sensor designs, fabrication schemes, wireless architectures, and patient trials reported here represent an advance in hydrocephalus diagnostics with ability to visualize flow in a simple, user-friendly mode, accessible to the physician and patient alike.

INTRODUCTION

Ventricular shunts represent an essential component of clinical treatment for hydrocephalus, a common and debilitating neurological disorder that results from the overproduction and/or impaired reabsorption of cerebrospinal fluid (CSF) produced in the ventricular system of the brain (*1*). Shunt assemblies typically involve two silicone catheters, connected upstream and downstream of a regulating valve, to drain excess CSF from the ventricle to a distal absorptive site. In this study, "ventricular shunt" refers to a shunt system consisting of a proximal catheter draining CSF from the ventricular system; a flow-, gravity-, or pressure-regulated valve; and a distal catheter draining fluid from the valve to the recipient site, such as the peritoneum, pleural cavity, or right atrium. Although effective in CSF diversion and prevention of the sequelae of hydrocephalus, shunts are highly prone to failure (*2*). Clinical symptoms of shunt malfunction tend to be nonspecific, such as headache, nausea, and somnolence, thereby creating challenges in clinical diagnosis (*3*, *4*). Because ramifications of misdiagnosis can include severe morbidity and mortality, accurately identifying shunt malfunction or failure is critical in the appropriate care of patients with hydrocephalus.

Diagnostic tests to assess shunt function include computed tomography (CT), plain films (x-ray), magnetic resonance imaging (MRI), radionuclide shunt patency studies (RSPSs; or "shunt-o-gram"), shunt aspiration, and flow monitoring systems (*5*–*7*). Each method, however, suffers from some combination of disadvantages, including excessive cost, poor reliability, low speeds, susceptibility to interference and patient discomfort, and potential for harm. CT scans and x-rays expose a vulnerable pediatric population to harmful radiation (1.57 ± 0.6 mSv and 1.87 ± 0.45 mSv, respectively). Shunted patients undergo an average of two CT scans annually that, over the course of the patient's lifetime, result in dangerous cumulative amounts of radiation exposure that have been linked to the onset of neurological and hematological malignancies (*8*, *9*). The MRI approach costs $3000 per study, the measurement can interfere with magnetic shunt valves, the availability is limited, and the wait times are typically long. Invasive testing in the form of RSPSs or simple aspiration is painful, time consuming, and potentially inaccurate and risks infection of the shunt system (*10*–*13*). Recent diagnostic entrants attempt to address these drawbacks but are limited by cumbersome, multistep protocols, in some cases including ice-mediated

[1]Frederick Seitz Materials Research Laboratory, Department of Materials Science and Engineering, University of Illinois at Urbana-Champaign, Urbana, IL 61801, USA. [2]Center for Bio-Integrated Electronics, Northwestern University, Evanston, IL 60208, USA. [3]Department of Materials Science and Engineering, Northwestern University, Evanston, IL 60208, USA. [4]Department of Neurological Surgery, Feinberg School of Medicine, Northwestern University, Chicago, IL 60611, USA. [5]AML, Department of Engineering Mechanics, Interdisciplinary Research Center for Flexible Electronics Technology, Tsinghua University, Beijing 100084, China. [6]Department of Electrical and Computer Engineering, University of Illinois at Urbana-Champaign, Urbana, IL 61801, USA. [7]Departments of Civil and Environmental Engineering, Mechanical Engineering, and Materials Science and Engineering, Northwestern University, Evanston, IL 60208, USA. [8]Feinberg School of Medicine, Northwestern University, Chicago, IL 60611, USA. [9]Department of Biomedical Engineering, Northwestern University, Evanston, IL 60208, USA. [10]Beckman Institute, University of Illinois at Urbana-Champaign, Urbana, IL 61801, USA. [11]Northwestern University Micro/Nano Fabrication Facility (NUFAB), Northwestern University, Evanston, IL 60208, USA. [12]Department of Radiology, Feinberg School of Medicine, Northwestern University, Chicago, IL 60611, USA.
*These authors contributed equally to this work.
†Corresponding author. Email: matthew.potts@nm.org (M.P.); jrogers@northwestern.edu (J.A.R.)

cooling, with equivocal or negative past clinical data (*5*, *7*, *14*, *15*). Ultimately, surgical intervention is required to assess and revise shunts in many patients. With risk of intraoperative complications and anesthetic exposure, gross procedural expenditures approach $67,000 per patient (*16*). Because a considerable proportion of such operations reveal shunt systems with proper flow profiles, these unnecessary procedures represent a large burden on the health care system.

Here, we present a simple, noninvasive sensor platform that provides a low-cost, comfortable means for quantitatively assessing flow through cerebrospinal shunts, continuously or intermittently. The system exploits advances in materials, mechanics, and fabrication schemes that serve as the foundations for a class of electronics that is ultrathin (h < 100 μm), soft (E ~70 kPa), lightweight (<10 mg/cm^2), and skin-like in its physical properties, with resulting flexural rigidities that are nine orders of magnitude lower than those of traditional, rigid sensors. Such epidermal electronic devices support clinical grade accuracy in capturing body kinematics (*17*), electrophysiological signals (*18*, *19*), soft tissue mechanical properties (*20*), and chemical markers in sweat (*21*, *22*), among others. Specific device constructions allow for high-resolution skin thermography and precise measurements of the thermal conductivity and the thermal diffusivity of the skin. We extended recent work in quantifying macrovascular blood flow based on measurements of spatial anisotropies in thermal transport (*23*) to generate a soft, skin-interfaced sensor that can accurately measure flow through cerebrospinal shunts in real time, in a noninvasive, quantitative, and wireless manner. Benchtop evaluations, thermographic imaging, and finite element analysis (FEA) of the physics of heat transport revealed the effects of skin thermal properties and thickness, as well as device and catheter geometries. The results establish considerations in design for a range of practical operating conditions. Trials on five adult shunt recipients with a diverse range of etiologies and comparisons with CT, MRI, and RSPSs validated device function in vivo, along with advanced processing algorithms for quantitative determination of flow rates.

RESULTS

Dense arrays for flow visualization

Previous work from our group showed that arrays of epidermal temperature sensors and thermal actuators could be used to quantify anisotropies in thermal transport induced by macrovascular blood flow through the skin (*23*, *24*). The epidermal sensing array (ESA) architectures and fabrication schemes used here increased the number of sensors by nearly a factor of 10, and the density of these elements by a factor of 4, using clusters distributed around a central thermal actuator to provide the precision and spatial resolution necessary for characterizing flow through shunts (Fig. 1, A and B).

Connecting unique combinations of rows (to supply a sensing voltage, V_{sup}) and columns (to measure a resulting current, I_{meas}) enabled individual addressing of each temperature-sensing element in the array (Fig. 1C). Operation of the thermal actuator (Fig. 1C) resulted in a spatiotemporal pattern of temperatures that was captured by high-speed, automated interrogation of the sensors in the array. Arrays in square geometries with an equal number of input and output lines (10 × 10) mitigated effects of parasitic current pathways, as shown by theoretical and experimental comparisons of current distributions in square and nonsquare arrays (fig. S1) for our system (fig. S2). The ease of fabrication and physical robustness (Fig. 1D) of metallic resistive sensor elements made them attractive options compared to semiconductor devices, composite organic thermistors, and others (*25*–*27*).

Thermal transport occurred most effectively along the direction of flow (Fig. 1E), thereby creating a pronounced anisotropy in the temperature distribution, with a magnitude that can be quantitatively related to the volumetric flow rate. The layout of the sensing elements allowed accurate measurements of this anisotropy for cases relevant to flow through subcutaneous shunts with typical dimensions.

Two regions of the ESA (upstream and downstream, referring to sensor position with respect to the flow direction and thermal actuator) each contained a set of 50 temperature sensors (Fig. 2A). Here, $U_{i,j}$ represents the temperature recorded by the upstream sensor at the ith row and jth column, and $D_{i,k}$ represents the downstream sensor at the ith row and kth column, where i ranges from 1 to 10 and j and k range from 1 to 5. The numbering for the jth column begins from the right, whereas the kth column begins from the left to maintain physical representation of sensor position (Fig. 2A). Temperature differentials ($\Delta T_{i,m} = D_{i,k} - U_{i,j}$; m ranges from 1 to 10) for each equidistant sensor pair with respect to the thermal actuator (where $j = k$, paired colors in Fig. 2A) define the degree of thermal anisotropy that results from flow. Values of ΔT for sensor pairs A and B, which directly overlaid the catheter, exhibited strong thermal anisotropy under two different flow conditions (0.02 and 0.2 ml/min) within an established range for CSF flow (Fig. 2B) (*28*). Sensor location B displayed a higher sensitivity to flow than location A because of the reduced effect of direct thermal conduction from the actuator, relative to anisotropic thermal transport due to fluid flow. Measurements of ΔT for distal sensor pairs orthogonal to the flow direction showed weak anisotropy (Fig. 2B, location C), whereas distal pairs parallel to the flow direction (Fig. 2B, location D) showed an absence of flow-induced thermal anisotropy. This orientation dependence obviated the requirement for precise sensor alignment to tube direction because of the ESA sensor density and cardinal symmetry.

A principal components analysis (PCA) model provided a facile method both for assessing catheter position with respect to the ESA ordinate system and for confirming the presence or absence of flow (Fig. 2C). The PCA model, constructed from a time series ESA measurement, used $\Delta T_{i,k}$ values to calculate the principal components (PC). $\Delta T_{i,k,t} = D_{i,k,t} - U_t$, where $D_{i,k,t}$ is the temperature for each sensor in the downstream sensor set at a particular time point (t) and U_t is the temperature at the same time point from a single upstream sensor. The first two components (PC1 and PC2) described about 92% of the overall variability of the data (PC1, 70.5%; PC2, 22.1%) with the remainder (8% across PC3:PC50) associated with noise. PCA biplots (Fig. 2C) show projections of each $\Delta T_{i,k,t}$ for two selected upstream sensors at each measurement in an ESA time series in two dimensions using the first two PCs. Data clustering (95% confidence ellipses) corresponding to three experimental conditions [absence of flow without thermal actuation (flow off/heat off), absence of flow with thermal actuation (flow off/heat on), and flow with thermal actuation with separate clusters for different flow regimes (0.02 and 0.2 ml/min)] shows that these clusters are independent of the selected U sensor (Fig. 2C and figs. S4 and S5). A comparison of the data clusters and PC shows that PC1 primarily relates to the degree of thermal actuation, whereas PC2 relates to the presence or absence of flow. Mapping the variables to the PCA biplot indicates sensor correlation to flow. An overlay of four variable factors corresponding to D sensors known to be proximal (red) and distal (blue) to fluid flow shows the

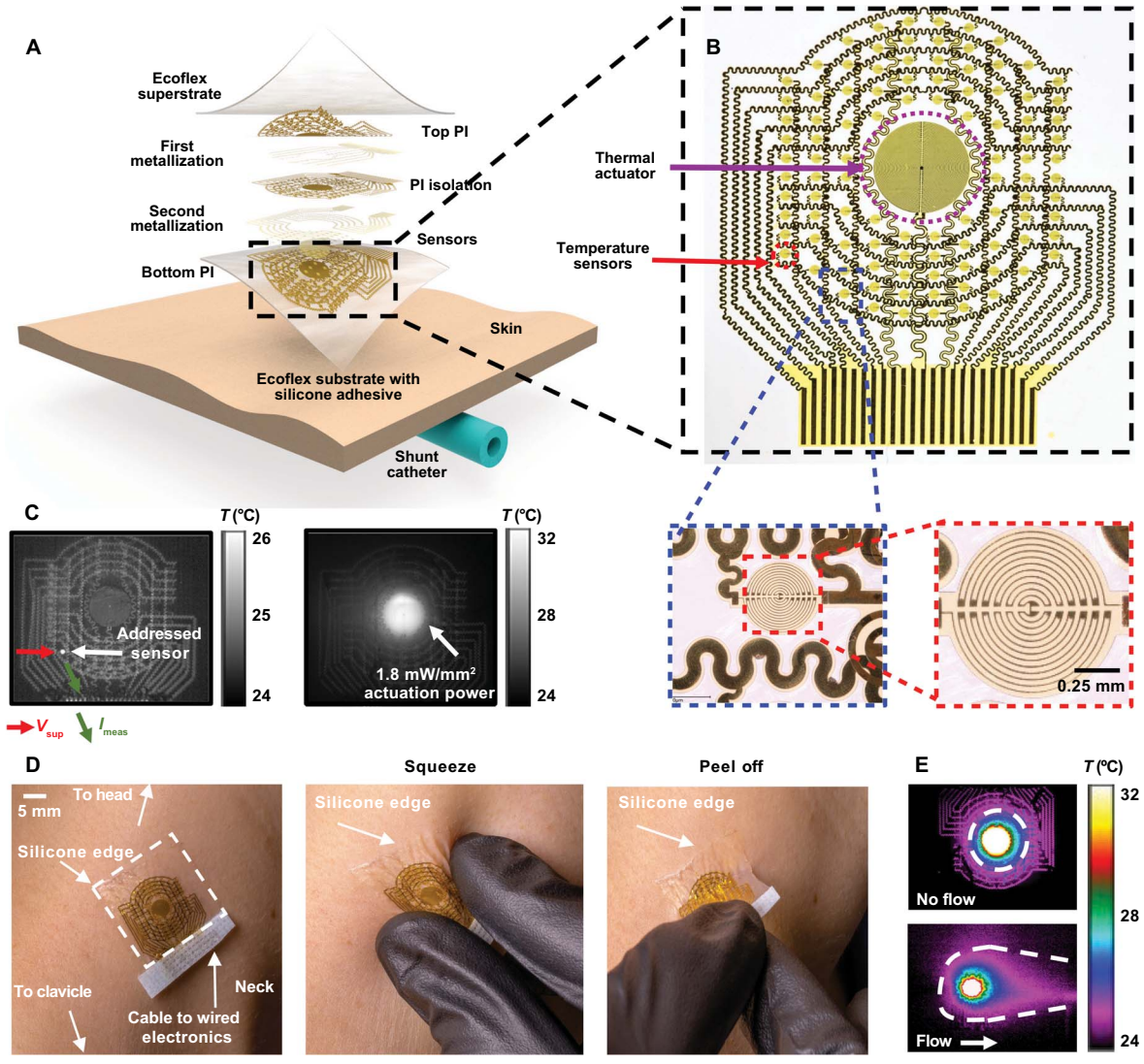

Fig. 1. Soft, skin-mounted wearable device for noninvasive, continuous, or intermittent measurement of flow through cerebrospinal shunts. (**A**) Exploded view illustration of a platform that incorporates a central thermal actuator surrounded by 100 precision temperature sensors, placed over the skin with an underlying shunt catheter. PI, polyimide. (**B**) Optical micrograph of the device, showing thermal actuator (surrounded by purple dashed line), with enlarged images showing stretchable, serpentine interconnects (bottom left, blue dashed line) and individual resistive temperature sensors (bottom right, red dashed line). (**C**) Infrared (IR) thermographs collected during measurement by an individual sensor (left), and thermal actuation with a power of 1.8 mW/mm^2, with representative voltage supply line (V_{sup}) and current measurement line (I_{meas}) marked in red and green, respectively. (**D**) Optical images of a device over a shunt during deformation to illustrate the robustness of the soft adhesion. Device was adhered to the skin on a seated subject 2 cm above the clavicle; the edge of the silicone substrate of the shunt is shown (arrows). (**E**) IR thermographs with color and contrast enhancement to highlight the spatial isotropy of the distribution of temperature in the absence of flow (top) and the anisotropy in the presence of flow (bottom). Flow is to the right (arrow).

positive and negative correlations to flow for the proximal and distal sensors, respectively, for both orthogonal and inline *U* sensors (Fig. 2C). PCA offers a strategy to mitigate effects of ESA misalignment by determining the *U* sensor that yields the maximum separation between no-flow and flow data clusters along the PC2 axis. The inline *U* sensor strongly separates these cluster groups as compared to the orthogonal *U* sensor (Fig. 2C). For scenarios without a priori orientation, PCA offers a straightforward means for evaluating correlations between *U* and flow state and, therefore, orientation of the catheter relative to the ESA.

The density of the ESA enabled spatial mapping of the temperature anisotropy that resulted from flow. These maps resulted from the processing of raw measurements from the ESA (Fig. 2D). First, by converting the raw ESA measurements (I_{meas}) to resistance and then temperatures by linear calibration [curve a priori established for each sensor of the ESA (see the "Spatial interpolation for heat maps" section in Supplementary Materials and Methods and fig. S6)], the temperature values can be mapped to the physical spatial coordinates of each sensor on a simulated square "pixel" array larger than the ESA (grid: 17 mm by 17 mm, 10 pixels mm^{-1}), resulting in a 170 by 170 by *N* matrix for a time series measurement of *N* frames. Conversion to $\mathbf{T}_{\mathbf{normalized}}$ results (bolded variables correspond to time series matrices) from the subtraction of the background temperature $T_{background}$ from each frame. The temperature map resulted from fitting a surface to

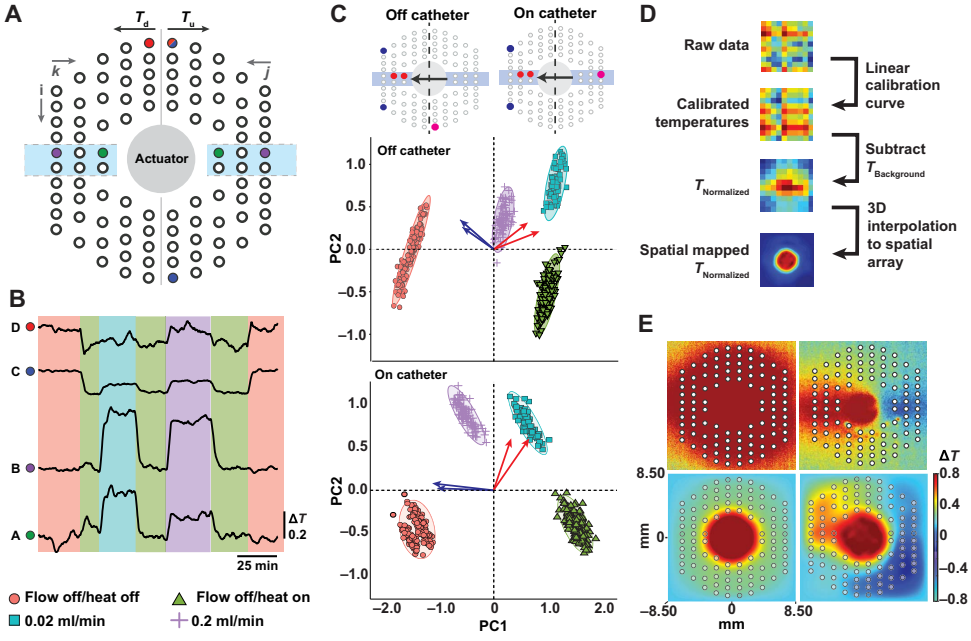

Fig. 2. Visualization of flow and measurements using an ESA. (**A**) Schematic map of a device, with indication of the tube position (blue shading), and the temperatures at upstream (T_u) and downstream (T_d) locations. *i*, *j*, and *k* represent coordinates for sensor identification (*j* and *k* for T_u and T_d, respectively). (**B**) Temperature differentials of four sensor pairs after baseline subtraction. Color coding in (A) denotes sensor locations. (**C**) PCA biplot (PC1 and PC2) of baseline-subtracted differentials between a selected T_u sensor (one off the catheter and one on the catheter as indicated) and each T_d sensor. Clustering occurs for the following cases: no flow and no actuation, no flow with actuation at 1.8 mW/mm^2, actuation at 1.8 mW/mm^2 and flow at 0.02 ml/min, actuation at 1.8 mW/mm^2, and flow at 2 ml/min. Vectors correspond to selected T_d sensors correlated positively (red) and negatively (blue) with flow. (**D**) Flow chart of the process for transforming raw ESA sensor data to spatially precise temperature maps. (**E**) Thermographs from IR imaging (top) and ESA-generated temperature maps (bottom) in the absence (left) and presence (right) of flow (0.02 ml/min; flow from right to left) with actuation at 1.8 mW/mm^2. All data were collected on a skin phantom.

the measured $\mathbf{T_{normalized}}$ values for each frame via meshed bicubic interpolation (boundary conditions $\mathbf{T_{normalized}} = 0$ from IR thermograph). Subtracting the actuator temperature and resulting isotropic heat transfer temperatures ($\mathbf{T_{actuator}}$) from $\mathbf{T_{normalized}}$ for every frame enhanced visualization of flow-induced anisotropic thermal transport. The high density of the ESA enabled good fidelity in visualizing the thermal anisotropy over the embedded catheter (Fig. 2D). Although experiments with patients do not typically allow for direct measurements of the flow and no-flow cases, theoretically derived or a priori measured "calibration" $\mathbf{T_{actuator}}$ facilitated the analysis (see the "Spatial interpolation for heat maps" section in Supplementary Materials and Methods).

Quantitative analysis of flow

Full mapping results obtained with the high-density ESA suggested means for simplifying the sensor to allow rapid measurements in a low-cost platform that consisted only of an actuator and a pair of sensors located 1.5-mm upstream ($T_{upstream}$) and downstream ($T_{downstream}$) of the actuator, respectively, which we refer to as an epidermal linear array (ELA; Fig. 3A). In this system, the actuator simultaneously served as a temperature sensor, and the measured temperature of the actuator, $T_{actuator}$, yielded a useful normalizing factor that facilitates data analysis independent of actuation power. Use of this system with a benchtop model allowed for the controlled exploration of the effects of flow, thermal, and geometric parameters (fig. S7). Operating the actuator at a controlled, low-power (1.35 mW/mm^2) setting created heat that diffused through the silicone skin phantom at a rate governed by the thermal diffusivity of this material, α_{skin}, with a characteristic penetration depth that can be expressed in the form of a dimensionless scaling law (fig. S8). Here, the phantom was treated as a semi-infinite solid (*29*) that approaches a quasi–steady-state equilibrium over relatively long (~400 s) times with a corresponding penetration depth of ~6 mm, although the thermal anisotropy was measurable well before this time, as the time taken to achieve 63.7% (τ) of the steady-state value is ~40 s (fig. S9). The transient sensor and actuator responses after actuation [$\Delta T_{sensors} = T_{sensor}(t) - T_{sensor}(t_{actuation})$; $\Delta T_{actuator} = T_{actuator}(t) - T_{actuator}(t_{actuation})$] for different flows ($Q_{CSF}$) appear in Fig. 3B. In the absence of flow ($Q_{CSF} = 0$), thermal transport from the actuator occurred equally in the $\pm x$,$\pm y$, and $-z$ directions, resulting in equal values for $\Delta T_{upstream}$ and $\Delta T_{downstream}$ (Fig. 3B, unshaded). The presence of flow led to a nonmonotonic effect on $\Delta T_{upstream}$ and $\Delta T_{downstream}$. At low flow rates (0 ml/min < Q_{CSF} < 0.05 ml/min), the fluid transported heat from the actuator preferentially to the downstream sensor and away from the upstream sensor, resulting in a measured increase in $\Delta T_{downstream}$, and decrease in $\Delta T_{upstream}$ (Fig. 3B, blue shading). The resulting thermal anisotropy, ~1 K, was two orders of magnitude above the temperature resolution of our sensors (0.02 K), as shown in extensive prior work (*27*). At higher flow rates (0.05 ml/min <Q_{CSF} <1 ml/min), the convective effects of the fluid dominated, leading to a net cooling effect on both sensors but at different rates, with $\Delta T_{upstream}$ equilibrating at a lower value than $\Delta T_{downstream}$ (Fig. 3B, orange and gray shading). The actuator was convectively cooled by the fluid at a rate governed by the magnitude of the flow, resulting in reductions of $\Delta T_{actuator}$ in the presence of flow (Fig. 3B, blue curve). These effects appear in the normalized quantities $T_{upstream}/T_{actuator}$ and $T_{downstream}/T_{actuator}$ (Fig. 3C). The nonmonotonic effects of flow for different skin thicknesses (h_{skin}) increased and decreased when considering the difference between the sensors ($\Delta T_{sensors}/T_{actuator}$) and their average ($\bar{T}_{sensors}/T_{actuator}$), respectively (Fig. 3, D and E). Here, $\Delta T_{sensors}/T_{actuator}$ and $\bar{T}_{sensors}/T_{actuator}$ were measures of thermal anisotropy and flow magnitude, respectively. Together, these quantities allowed for determination of flow rate and were used to distinguish degenerate points on either side of the peak values (Fig. 3D).

The thickness of the skin (h_{skin}) represents an important geometric parameter. Increasing h_{skin} decreases the effects of flow on the sensor responses, simply because of the finite depth of penetration of the thermal field (Fig. 3, D and E). Although transient techniques can be used to determine h_{skin} from thermal measurements, in practice, h_{skin} can be measured directly using CT and Doppler ultrasound. Typical ventricular catheters are implanted subcutaneously, as validated by radiographic and ultrasound imaging, at depths of 1 to 2 mm, within the range of detectability. Recent work (*30*) established a set of design considerations and algorithms for extracting depth-dependent thermal

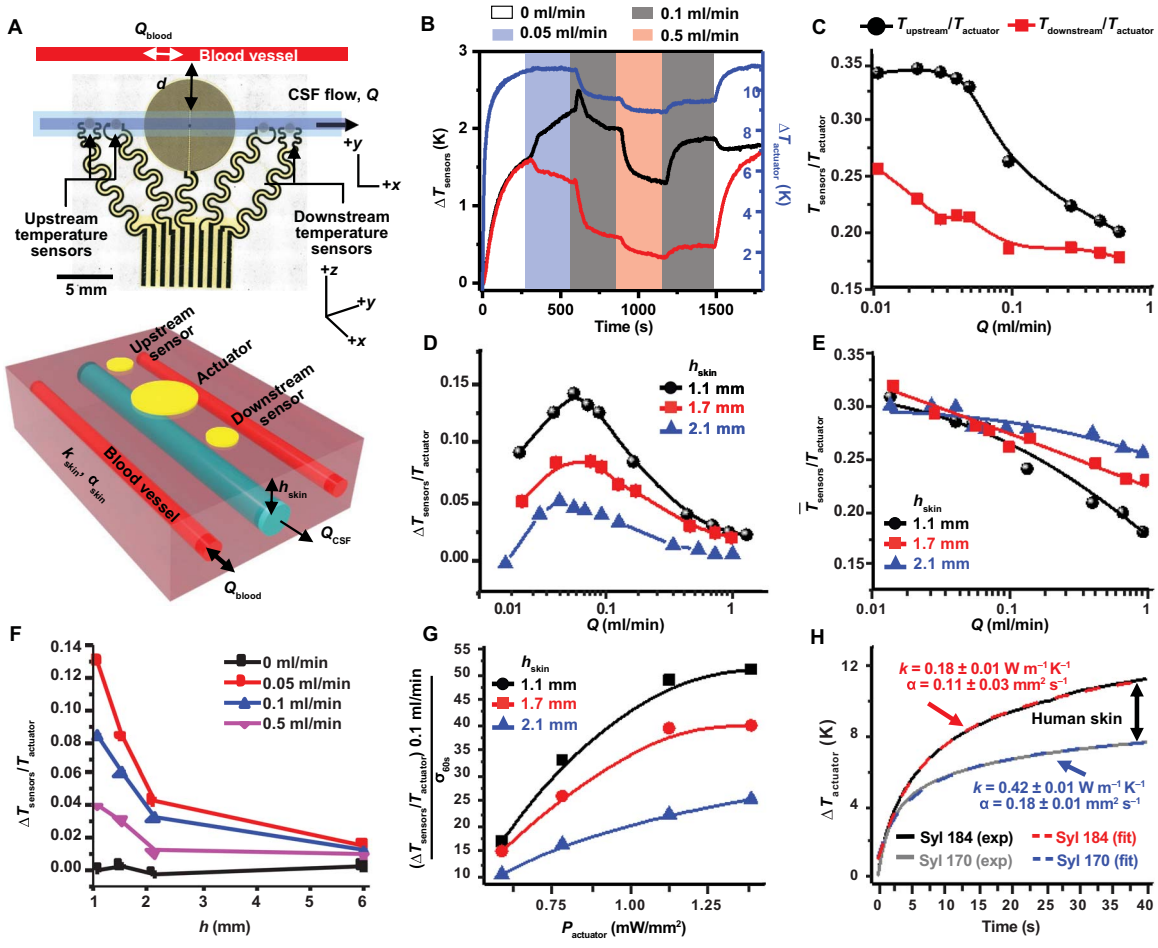

Fig. 3. Systematic characterization of the effects of geometry, thermal properties, and flow rates. (**A**) Optical image of ELA overlaid with an illustration of a catheter and a blood vessel (top) and schematic illustration of a benchtop system illustrating key features, including thermal properties of the skin phantom, CSF flow (Q_{flow}), and skin thickness (h_{skin}). (**B**) Temperatures measured after the onset of heating for the actuator (blue curve), the downstream sensor (black curve), and the upstream sensor (red curve) for four values of Q_{flow}: 0 ml/min (unshaded region), 0.05 ml/min (blue-shaded region), 0.1 ml/min (gray-shaded region), and 0.5 ml/min (orange-shaded region). (**C**) $T_{sensors}/T_{actuator}$ for the upstream (red curve) and the downstream (black curve) sensors across a range of flow rates from 0.01 to 0.1 ml/min. (**D**) $\Delta T_{sensors}/T_{actuator} = (T_{downstream} - T_{upstream})/T_{actuator}$ for a range of Q_{flow} from 0.01 to 0.1 ml/min for three anatomically relevant values of h_{skin}: 1.1 mm (black curve), 1.7 mm (red curve), and 2.1 mm (blue curve). (**E**) $\bar{T}_{sensors} = (T_{downstream} + T_{upstream})/2T_{actuator}$ for the same Q_{flow} and h_{skin} values as in (D). (**F**) In vitro experimental measurements of $\Delta T_{sensors}/T_{actuator}$ for h_{skin} (1.1, 1.7, 2.1, and 6.0 mm for four flow rates) and for Q_{flow} [0 ml/min (black curve), 0.05 ml/min (red curve), 0.1 ml/min (blue curve), and 0.5 ml/min (purple curve)]. (**G**) Ratio between signal ($\Delta T_{sensors}/T_{actuator}$) and noise (SD, σ) measured for Q_{flow} (0.1 ml/min) over a 60-s sampling window at a sampling frequency of 5 Hz, as a function of normalized actuator power for three different values of h_{skin} [1.1 mm (black curve), 1.7 mm (red curve), and 2.1 mm (blue curve)]. (**H**) In vitro experimental measurements (solid lines) and analytical fits (dashed lines) for $\Delta T_{actuator}$ as a function of time for $Q_{flow} = 0$ for two different skin phantoms, Sylgard 184 (black curve) and Sylgard 170 (gray curve) to simulate and measure human skin thermal properties (double-headed arrow). All data were collected on a skin phantom.

properties of soft tissue to depths of up to ~6 mm. To account for patients with varying habitus, or extreme skin thickness, we tested in vitro trials on our phantom skin assembly, which showed the ability of the ELA to make measurements at depths of up to 6 mm (Fig. 3F and fig. S10).

The power/area of the actuator ($P_{actuator}$) represents an important design consideration. Increasing $P_{actuator}$ improves the signal-to-noise ratio (SNR) of the measurements, but biological considerations set an upper limit for noninvasive use. The effects of $P_{actuator}$ on SNR appear in Fig. 3G, where the signal is an averaged measurement over 60 s (measured at 5 Hz) of $\Delta T_{sensors}/T_{actuator}$ for a flow rate of 0.13 ml/min. The noise is the SD (σ_{60s}) computed to three digits. At sufficiently high values of $P_{actuator}$ ($P_{actuator} > 1$ mW/mm^2), the advantages of increased actuation power diminished, and the noise stabilized at 2% of the measured signal. This power-invariant noise arises primarily from sampling noise inherent to the data acquisition system (DAQ) and from the time dynamic effects of convection. The effect of increased $P_{actuator}$ on $T_{sensors}$ and on $T_{actuator}$ appears in fig. S11, demonstrating (i) a linear relationship between $P_{actuator}$ and $T_{actuator}$ and (ii) the diminishing effects of increased $P_{actuator}$ on the measured ($T_{downstream} - T_{upstream}$).

The thermal conductivity (k_{skin}) and diffusivity (α_{skin}) of the skin also represent unknowns, with human skin exhibiting a range of 0.3 W m^{-1} K^{-1} < k_{skin} < 0.5 W m^{-1} K^{-1} and 0.07 mm^2 s^{-1} < α_{skin} < 0.15 mm^2 s^{-1} (*31*). Analytical curve fitting of the transient actuator temperature response, $\Delta T_{actuator}$, to well-studied functional forms (*32*) yielded these two quantities for two phantom skins (Fig. 3H) with thermal properties that bound this range. The measured values of $\Delta T_{sensors}/T_{actuator}$ were nearly identical for these two cases, whereas

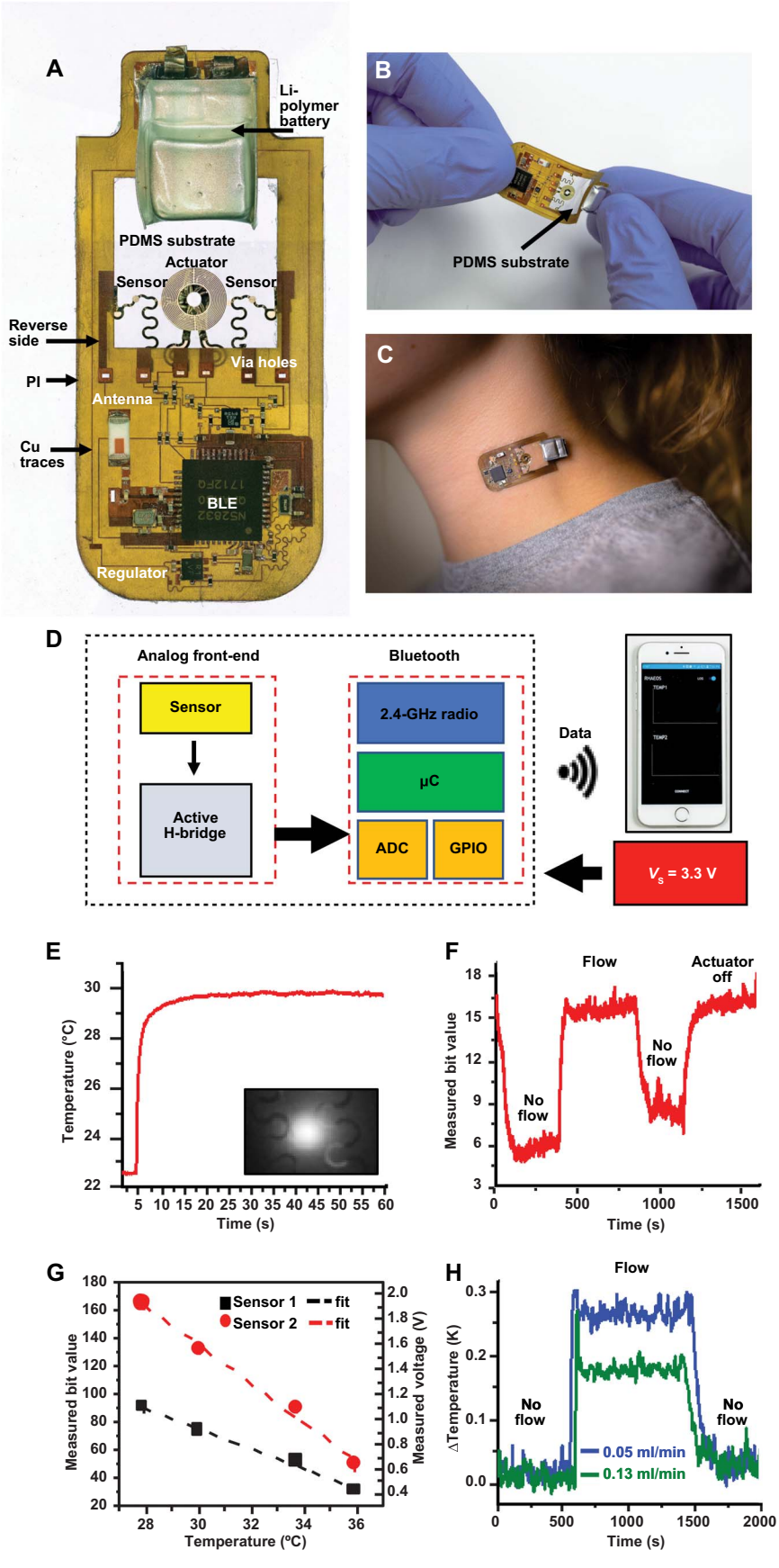

Fig. 4. Wireless data acquisition. (**A**) Optical micrograph of fully assembled, integrated wireless ELA showing soft, conformal sensing/actuating components, flex-PCB (Cu/PI/Cu), and surface-mounted electronic components. PDMS, polydimethylsiloxane. (**B**) Optical image of device bending, showing flexibility. (**C**) Optical image of device mounted on the skin using medical-grade, acrylate-based pressure-sensitive adhesive. (**D**) Schematic illustration of analog front-end, analog-to-digital converter (ADC), Bluetooth (BLE) transmission electronics, and 3.3-V power supply with custom smartphone application for real-time data readout and logging (right). (**E**) Raw sensor readout in measured bits from an 8-bit ADC during actuation and flow. (**F**) IR-measured temperature rise due to 3.6-mW actuation on the phantom shunt assembly. (**G**) Calibration curve to measure raw 8-bit, 3-V ADC values (left) and associated voltages (right) to temperatures via calibration. (**H**) Difference in $T_{upstream}$ and $T_{downstream}$ acquired wirelessly as a function of time for two different flows, $Q = 0.05$ ml/min and $Q = 0.13$ ml/min. All data were collected on a skin phantom.

the increased rates of thermal transport associated with Sylgard 170 increased the cooling effect of the fluid, thereby reducing the values of $\bar{T}_{sensors}/T_{actuator}$ (figs. S12 and S13). Ventricular catheters are constructed from standard medical-grade silicones, and their thermal properties were assumed to be known a priori ($k_{catheter}$ = 0.22 W m^{-1} K^{-1}, $\alpha_{catheter}$ = 0.12 mm^2 s^{-1}) (*33*). Last, catheter geometry and the thermal properties (k_{CSF} and α_{CSF}) of the CSF strongly influence the ultimate measurement, but they can also be assumed to be known a priori. A complete list of all thermal and geometric properties relevant to precise flow measurement, as well as their mode of acquisition, appears in table S1. Additional experiments quantified the convective heat transfer coefficient (H_{conv} = 20 W m^{-2} K^{-1}; fig. S14), the tolerance in positioning to achieve <20% error (20° rotational tolerance, 0.5-mm translational tolerance; fig. S15), the effect of sensor distance from the actuator (fig. S16), and the high- and low-frequency noise introduced by the DAQ as a function of sampling window, motion, convection, anisotropic conductive film (ACF) cable, and near-surface blood flow (figs. S17 to S21).

Wireless data acquisition via Bluetooth

Wireless data acquisition represents a key advance over previous demonstrations of epidermal temperature and flow sensors. Optical images of the wireless system demonstrate its flexibility and size (Fig. 4, A to C). The fabrication approach integrated soft, stretchable, low-modulus (~1 MPa) sensing components with flexible printed circuit boards (flex-PCBs) that offered the robustness required to support critical commercial wireless electronic components, such as batteries, Bluetooth chips, and power regulators. With a soft, easily removable skin-safe adhesive, this design afforded advantages

of epidermal electronics (low thermal mass and conformal contact) and the scalability of recent advances in flex-PCB manufacturing, yielding system-level flexibility and localized softness and stretch at the sensor. The entire system mounts on skin (Fig. 4C) via a medical-grade acrylate-based sheet adhesive, with an adhesion energy (880 N/m) higher than the work of adhesion required to induce delamination at 15% strain (~5 N/m), the yield strain of skin, while allowing for nonirritating contact and easy removal.

We constructed a customized temperature sensing and actuation circuit to perform wireless flow measurement (Fig. 4D). Subtle changes in resistance (<1 ohm) that resulted from changes in temperature appeared as changes in voltage (V_g) across the arms of a Wheatstone bridge. The total increase in temperature (~3 K) during actuation resulted in V_g < 10 mV, which is comparable to the resolution of an ADC with a 3.3-V range and 10-bit resolution (3.3 V/2^{10} = 3.2-mV resolution) and is lower than the resolution limit of an 8-bit ADC (3.3 V/2^8 = 12 mV). An operational amplifier amplified this signal across the 3.3-V range to achieve the required sensing resolution. The resistances of the nonsensing arms of the bridge can be tuned to bring the measured changes within the range of the ADC, and a custom circuit simulation allows for facile fine tuning of the circuit before assembly.

A Bluetooth communication protocol is attractive because of its long range and compatibility with standard smartphones and tablet computers. A commercially available Bluetooth transmitter digitized and transmitted this signal with 200-Hz sampling frequency to a custom smartphone application. A miniaturized, rechargeable, Li-polymer battery supplied power and was regulated by a low-dropout regulator, resulting in a stable, 3.3-V output. Thermal actuation resulted from voltage supply to the actuator, creating heating power that was facilely tuned via Wheatstone bridge calibration, and from voltage modulation through a general-purpose input/output (GPIO) pin. An example of this appears in Fig. 4E, with 3.6 mW of actuating power resulting in a localized temperature rise of 8 K on a silicone skin phantom. In vitro experiments demonstrated the effects of flow on measured temperatures (Fig. 4F), where the presence of flow (Q = 0.13 ml/min) through an underlying catheter resulted in a change in an adjacent sensor. Conversion of the raw, measured ADC values to temperature used a simple linear calibration (Fig. 4G) for two sensors on the same device, upstream and downstream of the catheter, acquired simultaneously with an 8-bit ADC. The utility of the system in performing wireless flow measurements is shown in Fig. 4H, where $T_{downstream} - T_{upstream}$ is shown for two flows as a function of time.

Near-term goals in clinical monitoring informed key device features. Fully assembled, the wireless ELA was 1.8 cm by 4.1 cm in size, with a thickness that varied by location (4 mm at the battery, ~100 μm everywhere else) and weighed 680 mg, with nearly half of this value from the battery (330 mg). During operation, the system consumed 6 mA of current. The rechargeable Li-polymer battery supplies 12 mAh at 4.2 V, resulting in a total working time of ~2 hours. Typical monitoring requires 5 min, resulting in battery life of ~6 days. The capacity can be readily increased via the use of a larger battery. The Bluetooth chip has 8 ADC pins, in addition to 20 GPIO pins, of which we use 2 and 1, respectively, suggesting straightforward pathways to expand the platform to realize fully wireless large-array sensors for complete spatial mapping using digital multiplexing schemes that use commercially available solid-state multiplexer/demultiplexer units (*34*). The functionality of the wired data transmission, recording, and power transmission electronics was entirely transferred to the miniaturized wireless design (fig. S22). Images and movies of the wireless system functioning via pairing with a smartphone application are shown in fig. S23 and movies S1 and S2, respectively.

Human studies for the evaluation of ventricular shunt function

Experiments on five shunt recipients with different pathologies demonstrated the clinical utility of the ELA measurement platforms. The device designs addressed three needs: (i) ease of handling for the surgeon to ensure facile placement and removal; (ii) comfort for the patient during application, operation, and removal; and (iii) robust mechanical and thermal coupling to the skin. The ELA had an ultrathin elastomer substrate (100 μm) supported by an elastomeric frame (2 mm; Fig. 5A). The devices adhered robustly and noninvasively to the skin, maintaining conformal contact with the skin even under extreme deformations. Successive measurements required placement on the skin over the distal catheter ("on shunt") and at a location adjacent to the distal catheter ("off shunt"; Fig. 5B). The off-shunt measurement had two key uses: (i) It served as a control for comparison to the on-shunt measurement, and (ii) it allows for the measurement of skin thermal properties without the influence of flow. Locating the catheter and positioning the ELA can typically be accomplished via touch in superficial regions, with further validation, as necessary, by hand-held Doppler ultrasound imaging (Fig. 5B, inset). Linear markings on the device allowed for easy alignment of the central axis of the actuator and sensors with the underlying shunt. Although the shunt was not visible under the skin, its ends were easily aligned to the markings on the device via touch. Low-power actuation (1.3 mW/mm^2) ensured maximum temperature increases of <5°C, which were confirmed by IR imaging (Fig. 5C). These values are below the threshold for sensation, in accordance with institutional review board (IRB)–approved protocols. Results showed a characteristic tear-drop distribution of temperature, consistent with the presence of flow.

The presence or absence of flow corresponding to shunt functioning or failure can be immediately determined simply by observing the presence or absence of thermal anisotropy. Measured values of $\Delta T_{sensors}/T_{actuator}$ (Fig. 5D) for on-shunt and off-shunt locations for all five patients revealed anisotropy for all working shunts. Details of each patient's etiologies and results are shown in table S2, and raw, measured values of $\Delta T_{sensors}/T_{actuator}$ and $\bar{T}_{sensors}/T_{actuator}$ for each patient are shown in table S3. Averaged values of $\Delta T_{sensors}/T_{actuator}$ at on-shunt and off-shunt locations, for cases with surgically or clinically confirmed flow, revealed differences (P = 0.012, n = 5) between measurements made in the presence and absence of flow, respectively (Fig. 5E, table S4, and raw readout in fig. S24). Images of the wired DAQ used for clinical studies appear in fig. S25; in vivo measurements of skin thermal properties appear in fig. S26; and simple validation studies on an external ventricular drain (EVD) appear in fig. S27.

Studies by x-ray, MRI, and CT imaging validated the ELA-derived measurements. Figure 6A corresponds to a patient (female, 36 years old) with a shunt malfunction suspected to be due to a kink in the distal catheter, which was confirmed by the x-ray and RSPS images. Surgical intervention relieved the kink, causing a visible increase in flow (Fig. 6B). The continuous presence of flow was further confirmed via postoperative x-ray and RSPSs, revealing a straightened distal catheter and a clear trace beyond the valve (Fig. 6C). Placement of the ELA at on-shunt and off-shunt locations, respectively, revealed no flow before the revision, consistent

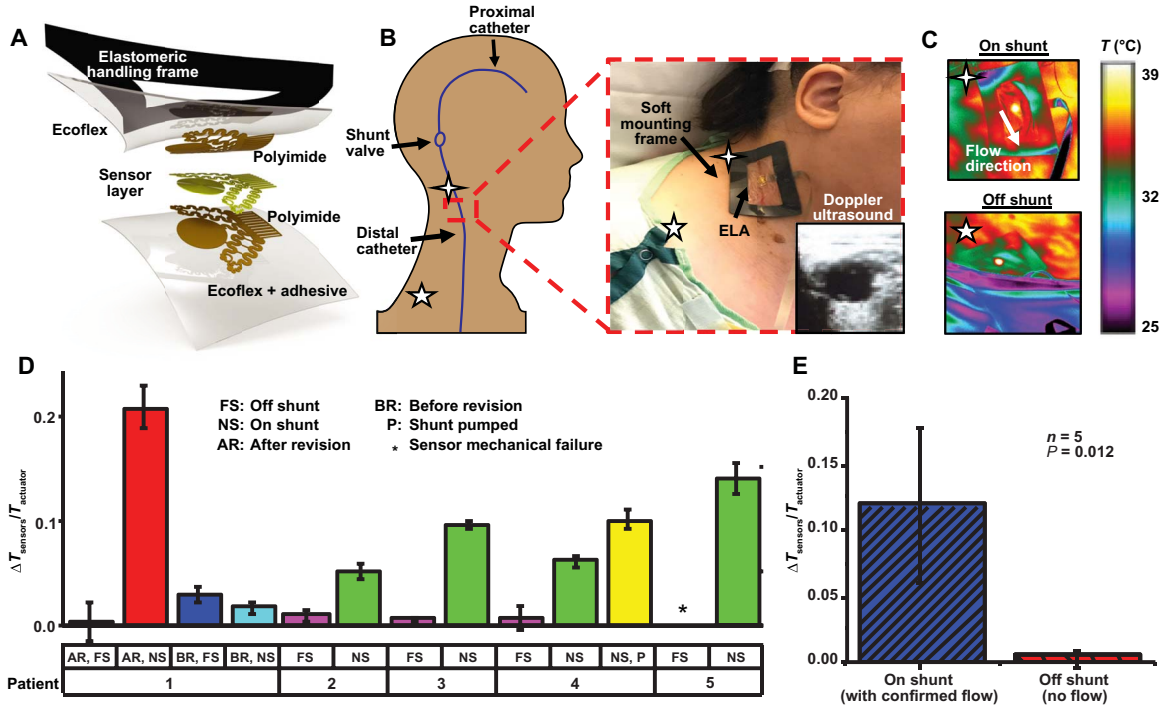

Fig. 5. Patient trials. (**A**) Exploded view illustration of an ELA designed for use in a hospital setting, with elastomeric handling frame and adhesive. (**B**) Illustration (left) and image (right) of on-shunt (⊹) and off-shunt (☆) ELA positioning on a patient, with representative Doppler ultrasound image (inset) of the catheter under the skin at the on-shunt location. (**C**) IR images at on-shunt (top) and off-shunt (bottom) locations indicating the local increase in temperature induced by the actuator, and characteristic teardrop-shaped heat distribution caused by the presence of flow. (**D**) Computed mean of $\Delta T_{sensors}/T_{actuator}$ measured for each patient at off-shunt and on-shunt location cases, with error bars representing SDs across a 100-sample window. (**E**) Computed mean of $\Delta T_{sensors}/T_{actuator}$ on $n = 5$ patients with clinically or surgically confirmed flow on off-shunt and on-shunt locations, with error bars representing SD. Statistical analysis was performed using a paired t test ($n = 5$) for cases with confirmed flow over on-shunt and off-shunt locations. Individual patient-level data and details of the paired Student's t tests are shown in table S5.

with x-ray and RSPS imaging. After operation, the off-shunt measurement showed no appreciable changes, whereas the on-shunt measurement showed the presence of flow (Fig. 6D).

The quantitative extraction of flow rates from such data can be accomplished via fitting to FEA models that use measurements of k_{skin} and α_{skin}, $\Delta T_{sensors}/T_{actuator}$, and $\bar{T}_{sensors}/T_{actuator}$ and a priori knowledge of the inner and outer diameters of the catheter and its thermal properties $k_{catheter}$ and $\alpha_{catheter}$ (Fig. 7A). k_{skin} and α_{skin} (measured in vivo as 0.29 W m^{-1} K^{-1} and 0.091 mm^2 s^{-1}, respectively) and h_{skin} (measured via CT imaging as ~1.43 and 1.52 mm on two patients, respectively; fig. S28) were inputs into an FEA model to generate curves for $\Delta T_{sensors}/T_{actuator}$ and $\bar{T}_{sensors}/T_{actuator}$. The experimentally measured values of $\Delta T_{sensors}/T_{actuator}$ and $\bar{T}_{sensors}/T_{actuator}$ fit to the computed curves yielded a nearly perfect match for a flow rate of 0.10 ml/min. In practice, experimental uncertainties in fitted values of h_{skin}, k_{skin}, and α_{skin} demand the use of multiparameter fitting models that treat the above quantities as fitting parameters within a fixed, defined range. Practically, the precise determination of subtle, real-time changes in flow through a shunt, as an indicator of healthy, intermittent, or obstructed flow, respectively, takes precedence over an accurate measurement of true flow rate. We detail a simplified approach that defines an effective flow rate, as measured by our sensor. Here, k_{skin} and α_{skin} assume known values, and calculations yield a family of FEA curves for different skin thicknesses. Iterative fitting of experimental data points to this set of curves yields a flow rate, with the self-consistency requirement that the experimental values match curves for $\Delta T_{sensors}/T_{actuator}$ and $\bar{T}_{sensors}/T_{actuator}$ at the same values of Q and h_{skin} (Fig. 7B).

In vivo data (Fig. 7C) demonstrated the utility of precise, effective flow rate measurements. Physician assessment and expected values of flow (*28*) for functioning and nonfunctioning shunts served as qualitative validation of these results. In patients 1 and 5, surgical observations confirmed our data. Assessments of patient 1 before corrective surgery indicated a shunt malfunction, consistent with ELA measurements (0.01 ± 0.01 ml/min). Measurements after a surgical revision revealed a flow rate of 0.06 ± 0.02 ml/min. Patients 2 and 3 were not suspected of shunt malfunction and exhibited flow rates of 0.36 ± 0.04 ml/min and 0.13 ± 0.02 ml/min, respectively, within established ranges for healthy CSF flow (*28*). Patient 4, initially measured to have occluded flow (0.013 ± 0.002 ml/min), had experienced severe and prolonged constipation for the week before the measurement and clinically deteriorated because of a likely pseudo-obstruction. Long-term constipation can decrease the resorptive ability of the peritoneum because of increased intraabdominal pressure and a decreased pressure gradient from ventricle to peritoneum (*35*). After administering a rigorous bowel regimen, the patient's mental status improved, and a subsequent measurement revealed healthy flow (0.16 ± 0.02 ml/min). Patient 5 was suspected to have shunt malfunction, and thermal measurements revealed highly occluded flow (0.027 ± 0.005 ml/min), which was later surgically confirmed. For these studies, the sensors were not used to make clinical determinations. In patients 4 (before bowel examination) and 5 (before surgery), the results of the measurements were blinded to the physician assessment (Fig. 7C). In a practical sense, uncertainties in these measurements can largely be eliminated by establishing baseline healthy flow for each patient, either immediately after operation or during a

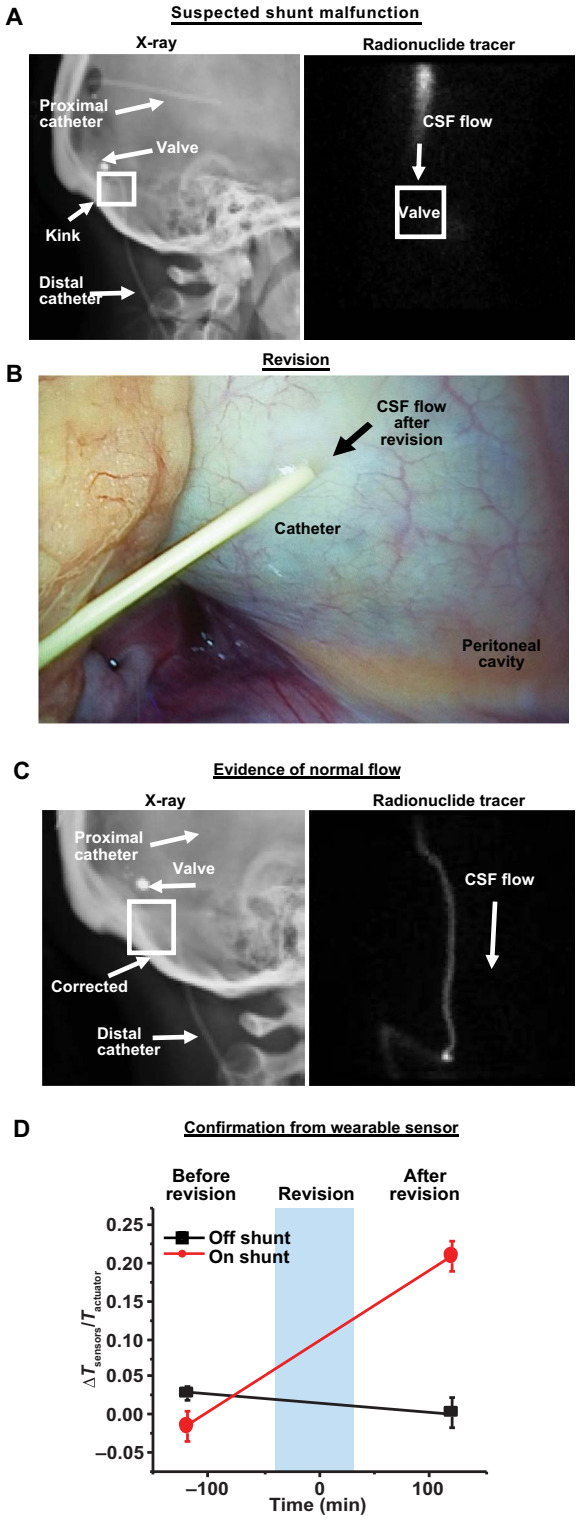

Fig. 6. Case study of a patient with hydrocephalus with shunt malfunction. (**A**) X-ray and radionuclide tracer showing kinking and occlusion of catheter. (**B**) Optical image of patient's peritoneal cavity immediately after surgery showing flow in repaired shunt. (**C**) X-ray and radionuclide tracer confirming proper operation of the repaired shunt. (**D**) $\Delta T_{sensors}/T_{actuator}$ measured by ELA at locations over (on) and adjacent to (off) the shunt before and after revision, confirming results from x-ray and radionuclide tracer. Blue shading indicates revision period. All data were collected on a patient ($n = 1$).

routine checkup, during which the patient is not suspected of shunt malfunction. In this way, relative changes in flow can easily be assessed without requiring precise flow rates, and follow-up measurements can distinguish between healthy flow, intermittent flow, obstructed flow, and total shunt failure. A computationally simple, multiparameter fitting model for true flow rate determination forms the basis of future work.

Measurement error, noise, and uncertainty

The noise inherent to the DAQ, together with factors that attenuate the signal such as the effects of skin thickness, convection, and in-plane heat dissipation, contributes to a total noise in benchtop flow measurements of $\Delta T_{sensors}/T_{actuator}$ of ~2% of signal in uncovered measurements, with detailed description of these noise sources appearing in the Supplementary Materials (see the "DAQ noise" in Supplementary Materials and Methods). In vivo measurements introduce noise due to motion of the subject that results in bending and deformation of the ELA and of the interface between the ultrathin, soft device and ACF cable. These effects appear in fig. S19, with optical images illustrating the ELA over deformed and undeformed skin as shown in fig. S19A. Time and frequency domain temperature data measured over 400 s on a stationary subject appear in fig. S19 (B to D), demonstrating primarily low-frequency natural temperature oscillations of 0.2 K, consistent with previous reports (*27*). Although convection could pose another potential source of noise, this affects both sensors and the actuator equally, and as such, these changes will largely disappear in analysis approaches that rely on differentials between these two quantities. Deliberate deformation results in characteristic noise associated with vigorous motion, gentle motion, strain on the ELA, and complete delamination, as shown in fig. S19 (E to G). In practice, mechanical motions of the ACF cable and induced stresses/strains at the soft bond pads created by motions of the patient are the primary sources of noise, which we measure in vivo, on average, to be 9 to 10% of the measured $\Delta T_{sensors}/T_{actuator}$ signal for all patients (on on-shunt locations). Elimination of the ACF cable, through wireless embodiments, or enhancements of its interfaces to the bond pad with soldered connections may mitigate these effects.

Altered intersensor distances due to the stretchability of the sensor represent another source of uncertainty. The peak sensitivity to flow changes occurs at $L = 2.5$ mm upstream and downstream from the edge of the actuator (fig. S16). Uniaxial strain of 15% (the yield strain of skin) at this distance corresponds to a positional uncertainty of ±0.375 mm, and although this results in an uncertainty in flow determination of ~10%, it does not compromise the ability to unambiguously determine the presence or absence of flow. In addition, our use of a medical-grade adhesive silicone ensured that the sensor did not move laterally in relation to the catheter. A complete discussion of the technical challenges faced during the clinical trials and their solutions is shown in table S5.

Comparison to recent technologies

A commercially available sensor (ShuntCheck) offers an alternative to imaging-based diagnostic tools (*5*, *7*, *14*, *36*). The system comprises a cooling pack that is held against the skin over the distal catheter, with conventional, bulk temperature sensors attached to the skin downstream, along the direction of the catheter. The pack cools flowing CSF, thereby decreasing the temperature of the downstream sensor. Although this system has high specificity

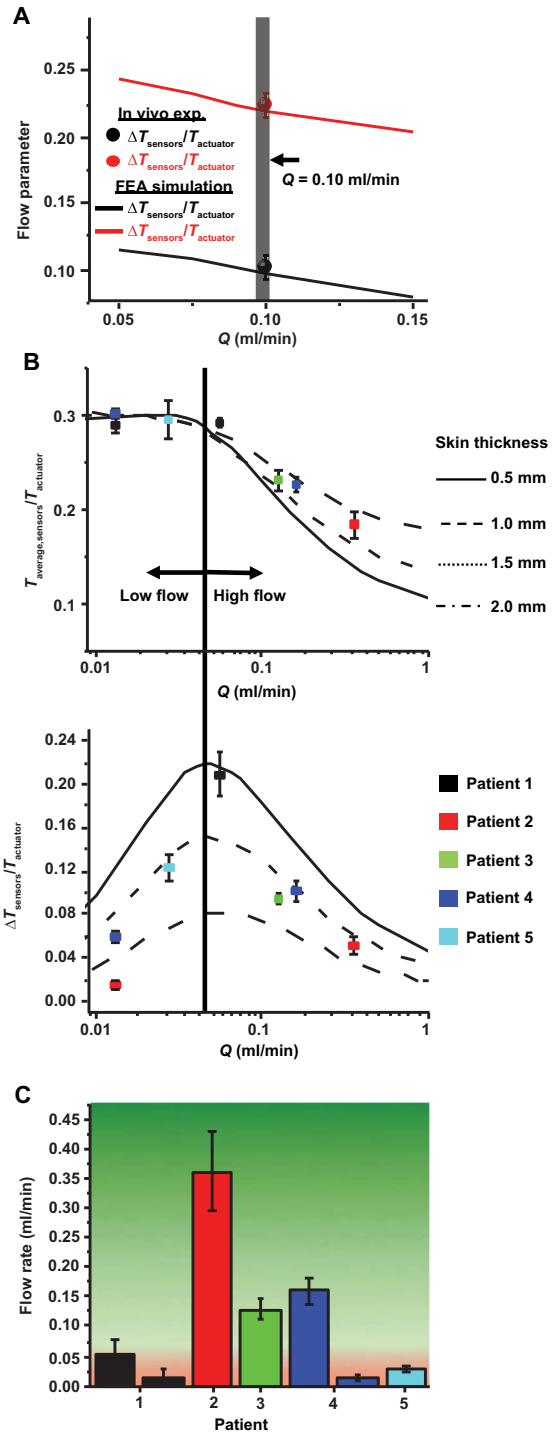

Fig. 7. Computation of flow rates. (**A**) FEA-computed values of $\Delta T_{sensors}/T_{actuator}$ and $\bar{T}_{sensors}/T_{actuator}$ using values of h_{skin} = 1.5 mm (acquired from CT imaging) and k_{skin} = 0.29 W m^{-1} K^{-1} and α_{skin} = 0.091 mm^2 s^{-1} acquired in vivo from a patient as shown in Fig. 5, overlaid with experimentally measured points from the same patient, yielding a flow rate of 0.1 ml/min. (**B**) FEA-computed family of curves of $\Delta T_{sensors}/T_{actuator}$ (top) and $\bar{T}_{sensors}/T_{actuator}$ (bottom) for different skin thicknesses with data measured in vivo from each patient, assuming k_{skin} = 0.32 W m^{-1} K^{-1} and α_{skin} = 0.1 mm^2 s^{-1}. (**C**) Computed flow rates from iteratively solving for both $\Delta T_{sensors}/T_{actuator}$ and $\bar{T}_{sensors}/T_{actuator}$. The error bars represent average differences in the individual values yielded by the two curves, and the colored background identifies ranges of healthy flow (green) and failure (red). All data were collected on patients (n = 5).

(~100%) (*7*) and sensitivity (80%), it suffers from key limitations. First, the embodiment is bulky and offers a poorly coupled sensor-skin interface that demands the use of a large pack (2.5 cm by 2.5 cm) and significant cooling. This requirement, together with a conventional, large-scale DAQ, decreases the usability of the system and prevents continuous, long-term measurements, precluding the ability to measure intermittent flow and to use patients' past data as a reference. Second, the measurements are semiquantitative, without an ability to account for key factors such as skin thickness, skin thermal properties, and device layout. Together, these factors lead to overall patient discomfort and prevent straightforward interpretation of data (*7*). A comparison of existing diagnostic techniques is shown in table S6.

DISCUSSION

The goal of the study was to validate our sensor's performance through a range of in vitro and in vivo testing. In vitro testing yielded the effects of key physical variables, such as varying flow rates, skin thicknesses, and actuating power, whereas in vivo tests provided insights into both device performance and practical aspects such as device handling and ease of use. The sensor was able to capture differences between cases with flow and no flow (P = 0.012) in vivo, as validated clinically by either imaging or surgical evaluation.

Detailed descriptions of patient trials

Consistent with early adoption of any novel technology, there was a learning curve associated with locating the tunneled distal shunt tubing, manipulating the device, identifying an ideal placement location, appropriately laminating the device to the patient, maintaining patient position, and preventing patient motion with resultant noise artifact generation. However, thoughtful modifications based on feedback after the first patient study resulted in rapid improvements.

Connecting the proximal and distal sites of shunt tubing generally involves tunneling the catheter subcutaneously. In the case of peritoneal catheters, this is accomplished by a surgeon operating proximally at the cranial aspect of the patient, passing a long, sharp trocar containing distal shunt tubing under the skin from the incision, maneuvering it over the clavicle, and then placing it with a recipient surgeon to be inserted into peritoneum. This tubing is connected to the valve assembly, which is then connected to the proximal catheter. Flow is confirmed through the system after all lines are flushed of air and CSF drainage commences. Tunneling of the catheter occurs above the clavicle to prevent inadvertent complications from piercing the thoracic viscera, including the lung, mediastinum, and heart. It is at this point that the catheter is uniformly superficial (<2 mm) in most shunted patients.

After location of optimal sensor placement site, handling the device was problematic during the initial patient trial. As a soft, flexible device lined with adhesive, it lined to surgeon hands, was difficult to align with the underlying shunt tubing, and delaminated with factors including patient movement, repetitive device uses, and repositioning. Alignment relied on positioning the central core of the sensor over the shunt tubing, which proved problematic with an adherent device. Further, inappropriate handling led to mechanical destruction of the underlying electronics, leading to aberrant readings. All of these problems were addressed after one substantive device improvement was performed, improving its efficacy throughout the duration of the subsequent patient trials.

The redesign of the device considered many of factors, largely focusing on enclosure and adhesive capabilities. An elastomeric enclosure was laser-structured and added to the sensor as a handling frame. This achieved two marked performance improvements: First, by confining the adhesive to a limited area, a barrier was created between the sensor and the surgeon's gloves, minimizing challenges associated with handling. Second, by marking lines corresponding with the central axis of the sensor, the surgeon's device placement became straightforward after the localization of the tunneled distal catheter tubing. Clinical-grade adhesive silicone ($Q_{adhesion}$ = 160 N/m; MG 1010, Dow Corning) was also applied to the underside of the device, which permitted secure initial placement and weathered patient movement and multiple uses. This had no effect on the superficial skin, with no skin irritation noted nor expressed by trial subjects.

As positionality is a variable with known effect on shunt performance, it was controlled by examining all patients upright in their hospital bed. Maintaining this position was challenging in certain patients because of factors including boredom, discomfort, postsurgical or chronic pain, and cognitive disability. The presence of family members often helped with these challenges, offering conversation, empathy, or advice to allow for trials to run unencumbered. As an unintended side effect, in all successive trials, patient family members and caregivers expressed enthusiasm for the sensor's design and form factor.

Last, we noted motion noise during patient movement. These movements ranged from normal respirations to positional shifts due to the factors listed above, with detailed descriptions in Results. After examination of the device and its components, it was noted that the predominance of noise-related issues transpired because of fluctuations in the ACF cables used. This prompted the development of the wireless device iteration.

Certain unusual circumstances over the course of the patient trials warrant further discussion. After initial surgical shunt placement, patient 4 was noted to subjectively cognitively deteriorate by nursing staff. A sensor reading was obtained during this period, although the study team attributed these symptoms initially to recovery from anesthetic. No flow was ascertained during this measurement. When the patient became further obtunded and unarousable, it was revealed that the patient had not stooled in 1 week, with an abdominal x-ray performed displaying a substantive stool burden. A laxative regimen was administered overnight, and a follow-up sensor reading demonstrated normal catheter flow. This was congruent with the known phenomena of pseudomalfunction, wherein severe constipation, urinary tract infection, and inability to void have clinically produced the clinical symptoms of shunt malfunction. Further research is necessary to provide exact specifics as to the nature and mechanics of these malfunctions, but it was interesting to quantitatively capture this phenomenon in real time. Last, patient 5 was suspected to have shunt malfunction and had been recently admitted for a surgical revision. However, a preoperative sensor measurement revealed the presence of occluded flow that was confirmed hours later over the course of surgery.

Limitations of our study

For robust, reliable clinical shunt monitoring, we recognize the need for careful validation to study a range of long-term factors, such as body habitus, collagen scar tissue formation, or calcification of the shunt, and how they interfere with our measurements. However, to a reasonable approximation, these changes will affect the upstream and downstream temperature sensor equally, and as such, these changes will largely disappear in analysis approaches that rely on differentials between these two quantities. In addition, although we were able to detect statistically significant ($P < 0.05$) differences in cases with (on shunt) and without (off shunt) flow, respectively, the low sample size represents an important caveat and suggests the need for a larger-scale study to further validate our findings. Last, we recognize the need for clinical validation of our wireless embodiment, which, along with the need for larger sample size, informs the design of a larger clinical trial based entirely on the wireless embodiment.

Implications for hydrocephalus treatment and research

Overall, the skin-like, precision sensor systems introduced here have the potential to represent a paradigm shift in clinical diagnostics of shunt malfunction. Compared to radiographic imaging, invasive sampling, and ice pack cooling, these platforms are unique in their integration of precision, soft, thermal sensors with wireless transmission capability. By exploiting advanced concepts in the measurement of thermal anisotropy and skin-conformal epidermal electronics, these devices can provide further quantitative modes of use beyond opportunities afforded by the embodiment studies here. For example, comparison of measured, quantitative flow rates from the ELA can be used in conjunction with a manufacturer-supplied calibration chart to measure intracranial pressure. In addition, prior work (*23*) has established the suitability of related device in measurements of near-surface blood flow, which can be applied to study neural blood supply. Many poorly understood conditions stem from neurological hydrodynamic dysfunction, including normal pressure hydrocephalus and idiopathic intracranial hypertension. By understanding individual flow rates in these conditions, novel and improved treatment approaches can potentially be developed for their care.

MATERIALS AND METHODS

Study design

The goals of the study were to design and fabricate our novel, soft epidermal sensors and to validate their performance against clinician diagnosis, surgical observation, and imaging results. Patients were recruited from the population of the study site (Northwestern Memorial Hospital, Chicago, IL; IRB protocol STU0020542). Inclusion criteria specified patients with previously implanted ventricular shunts undergoing evaluation or routine follow-up and patients undergoing new ventricular shunt placement procedures. The study was not formally blinded, although sensor measurements were performed and analyzed without previous knowledge of imaging or surgical results. Patients were evaluated at a 45° angle during device placement. Sensor placement was determined on the basis of touch to locate the most superficial location of the shunt, either over the clavicle or on the neck. A single measurement consisted of placing the sensor on the skin and waiting for 60 s for the sensor to equilibrate with the skin. Low-power thermal actuation (1.6 mW/mm^2) was then supplied for 240 s and then halted for the next 120 s, while making continuous temperature measurements of both the sensors and the actuator. All data recording occurred at 5 Hz, and all data processing used an adjacent-averaging filter with a 10-point sampling window. Two successive measurements each were made on the skin directly overlying the shunt and at a skin location adjacent to the shunt. The shunt was easily located, and alignment marks on the device allowed for easy alignment. An elastomeric enclosure around the device facilitated handling of the device. Details of each patient and their etiologies appear in table S2, and individual patient-level data are shown in table S3.

Statistical analysis

Data are presented with average values and SD, unless noted in the figure caption. Paired *t* tests performed on SPSS (IBM Inc.) compared thermal measurements in the presence and absence of flow. PCAs of the ESA data were performed using the R statistical language. Linear regression analysis of measured sensor data was used to generate temperature calibration curves for all sensors and to determine thermal conductivity using MATLAB. Quantitative flow analysis was conducted on measured data via fitting analysis in MATLAB using numerical relationships calculated via Finite Element Modeling (ABAQUS).

SUPPLEMENTARY MATERIALS

www.sciencetranslationalmedicine.org/cgi/content/full/10/465/eaat8437/DC1

Materials and Methods

Fig. S1. Current pathways through resistive arrays.

Fig. S2. Schematic illustration of the DAQ and control system for an array of 100 sensors.

Fig. S3. Calibration map for ESA.

Fig. S4. PCA for determining the presence of flow with an ESA.

Fig. S5. PCA for determining the orientation and magnitude of flow with an ESA.

Fig. S6. Flow diagram detailing the process for conversion of raw ESA sensor recordings to a spatial temperature map.

Fig. S7. Benchtop flow system.

Fig. S8. Depth of thermal penetration.

Fig. S9. Transient thermal analysis of flow.

Fig. S10. Flow measurements through thick (6 mm) layers of soft tissue.

Fig. S11. Effect of actuator power.

Fig. S12. Experimentally measured effects of changing skin thermal properties.

Fig. S13. Simulated effects of changing skin thermal properties.

Fig. S14. Effect of ambient free air convection.

Fig. S15. Effect of uncertainty in placement.

Fig. S16. Effect of altered intersensor distances.

Fig. S17. Low-frequency dc noise sources.

Fig. S18. High-frequency ac and dc noise.

Fig. S19. In vivo noise.

Fig. S20. Prevention of delamination during extreme deformation via adhesive design.

Fig. S21. Effect of near-surface blood vessels.

Fig. S22. Wired and wireless DAQ and control systems.

Fig. S23. Wireless control via smartphone.

Fig. S24. Wired DAQ used in clinical trials.

Fig. S25. Raw in vivo data.

Fig. S26. In vivo measurements of skin thermal properties.

Fig. S27. Measurements made over EVD.

Fig. S28. In vivo measurements of skin thickness made via radiographic and ultrasound imaging.

Table S1. Thermal and geometrical quantities required for quantitative measurement of flow rate.

Table S2. Summary of etiology of and measurements made on each patient.

Table S3. Raw data measured on each patient.

Table S4. Raw data and results from paired *t* tests for on-shunt and off-shunt measurements for patients with patent shunts.

Table S5. Summary of technical challenges and key advancements over the course of patient study.

Table S6. Summary of existing shunt diagnostic tools.

Movie S1. Wireless ELA pairing to smartphone app and on-demand actuation.

Movie S2. Experimental system in movie S1.

REFERENCES AND NOTES

1. R. A. Rachel, Surgical treatment of hydrocephalus: A historical perspective. *Pediatr. Neurosurg.* **30**, 296–304 (1999).
2. J. Tervonen, V. Leinonen, J. E. Jääskeläinen, S. Koponen, T. J. Huttunen, Rate and risk factors for shunt revision in pediatric patients with hydrocephalus—A population-based study. *World Neurosurg.* **101**, 615–622 (2017).
3. M. Kirkpatrick, H. Engleman, R. A. Minns, Symptoms and signs of progressive hydrocephalus. *Arch. Dis. Child.* **64**, 124–128 (1989).
4. J. H. Piatt Jr., H. J. L. Garton, Clinical diagnosis of ventriculoperitoneal shunt failure among children with hydrocephalus. *Pediatr. Emerg. Care* **24**, 201–210 (2008).
5. T. P. Boyle, R. Keating, J. Chamberlain, D, M. Frim, P. Zakrzewski, P. M. Klinge, L. H Merck, J. H. Piatt, J. E. Bennett, D. I. Sandberg, F. A. Boop, J. R. Madsen, J. J. Zorc, M. I. Neuman, M. S. Tamber, R. W. Hickey, MD3, G. G. Heuer, J. R. Leonard, J. C Leonard, ShuntCheck versus Neuroimaging for Diagnosing Ventricular Shunt Malfunction in the Emergency Department, paper presented at the Annual Meeting of the Pediatric Academic Societies, San Francisco, California, May 2017.
6. A. N. Wallace, J. McConathy, C. O. Menias, S. Bhalla, F. J. Wippold II, Imaging evaluation of CSF shunts. *AJR Am. J. Roentgenol.* **202**, 38–53 (2014).
7. J. R. Madsen, G. S. Abazi, L. Fleming, M. Proctor, R. Grondin, S. Magge, P. Casey, T. Anor, Evaluation of the ShuntCheck noninvasive thermal technique for shunt flow detection in hydrocephalic patients. *Neurosurgery* **68**, 198–205 (2011).
8. K. Koral, T. Blackburn, A. A. Bailey, K. M. Koral, J. Anderson, Strengthening the argument for rapid brain MR imaging: Estimation of reduction in lifetime attributable risk of developing fatal cancer in children with shunted hydrocephalus by instituting a rapid brain MR imaging protocol in lieu of head CT. *AJNR Am. J. Neuroradiol.* **33**, 1851–1854 (2012).
9. S. Krishnamurthy, B. Schmidt, M. D. Tichenor, Radiation risk due to shunted hydrocephalus and the role of MR imaging–safe programmable valves. *AJNR Am. J. Neuroradiol.* **34**, 695–697 (2013).
10. A. J. Brendel, S. Wynchank, J. P. Castel, J. L. Barat, F. Leccia, D. Ducassou, Cerebrospinal shunt flow in adults: Radionuclide quantitation with emphasis on patient position. *Radiology* **149**, 815–818 (1983).
11. D. Ouellette, T. Lynch, E. Bruder, E. Everson, G. Joubert, J. A. Seabrook, R. K. Lim, Additive value of nuclear medicine shuntograms to computed tomography for suspected cerebrospinal fluid shunt obstruction in the pediatric emergency department. *Pediatr. Emerg. Care* **25**, 827–830 (2009).
12. L. Uliel, V. M. Mellnick, C. O. Menias, A. L. Holz, J. McConathy, Nuclear medicine in the acute clinical setting: Indications, imaging findings, and potential pitfalls. *Radiographics* **33**, 375–396 (2013).
13. O. Vernet, J.-P. Farmer, R. Lambert, J. L. Montes, Radionuclide shuntogram: Adjunct to manage hydrocephalic patients. *J. Nucl. Med.* **37**, 406–410 (1996).
14. R.V. Recinos, E. Ahn, B. Carson, G. Jallo, Shuntcheck, A non-invasive device to assess ventricular shunt flow: One institution's early experience (abstract 1-1), *Am. Assoc. Neurol. Surg*. (2009).
15. D. M. Frim, T. Boyle, J. Zorc, R. Hickey, M. Neuman, J. Chamberlain, G. Heuer, R. Boop, D. Sandberg, T. Mandeep, P. Klinge, L. Merck, R. Keating, J. Leonard, J. Piatt, J. Bennett, D. Chesler, M. Hameed, T. Anor, F. Fritz, J. Madsen, Thermal flow detection improves diagnostic accuracy of shunt malfunction: Prospective, multicenter, operator-blinded study (abstract 1-2), *Am. Assoc. Neurol. Surg*. (2017).
16. A. Kutscher, U. Nestler, M. K. Bernhard, A. Merkenschlager, U. Thome, W. Kiess, S. Schob, J. Meixensberger, M. Preuss, Adult long-term health-related quality of life of congenital hydrocephalus patients. *J. Neurosurg. Pediatr.* **16**, 621–625 (2015).
17. S. Xu, Y. Zhang, L. Jia, K. E. Mathewson, K.-I. Jang, J. Kim, H. Fu, X. Huang, P. Chava, R. Wang, S. Bhole, L. Wang, Y. J. Na, Y. Guan, M. Flavin, Z. Han, Y. Huang, J. A. Rogers, Soft microfluidic assemblies of sensors, circuits, and radios for the skin. *Science* **344**, 70–74 (2014).
18. J. J. S. Norton, D. S. Lee, J. W. Lee, W. Lee, O. Kwon, P. Won, S.-Y. Jung, H. Cheng, J.-W. Jeong, A. Akce, S. Umunna, I. Na, Y. H. Kwon, X. Q. Wang, Z. Liu, U. Paik, Y. Huang, T. Bretl, W.-H. Yeo, J. A. Rogers, Soft, curved electrode systems capable of integration on the auricle as a persistent brain–computer interface. *Proc. Natl. Acad. Sci. U.S.A.* **112**, 3920–3925 (2015).
19. J. Kim, A. Banks, H. Cheng, Z. Xie, S. Xu, K. I. Jang, J. W. Lee, Z. Liu, P. Gutruf, X. Huang, P. Wei, F. Liu, K. Li, M. Dalal, R. Ghaffari, X. Feng, Y. Huang, S. Gupta, U. Paik, J. A. Rogers, Epidermal electronics with advanced capabilities in near-field communication. *Small* **11**, 906–912 (2015).
20. C. Dagdeviren, Y. Shi, P. Joe, R. Ghaffari, G. Balooch, K. Usgaonkar, O. Gur, P. L. Tran, J. R. Crosby, M. Meyer, Y. Su, R. Chad Webb, A. S. Tedesco, M. J. Slepian, Y. Huang, J. A. Rogers, Conformal piezoelectric systems for clinical and experimental characterization of soft tissue biomechanics. *Nat. Mater.* **14**, 728–736 (2015).
21. J. Choi, D. Kang, S. Han, S. B. Kim, J. A. Rogers, Thin, soft, skin-mounted microfluidic networks with capillary bursting valves for chrono-sampling of sweat. *Adv. Healthc. Mater.* **6**, 1601355 (2017).
22. A. Koh, D. Kang, Y. Xue, S. Lee, R. M. Pielak, J. Kim, T. Hwang, S. Min, A. Banks, P. Bastien, M. C. Manco, L. Wang, K. R. Ammann, K.-I. Jang, P. Won, S. Han, R. Ghaffari, U. Paik, M. J. Slepian, G. Balooch, Y. Huang, J. A. Rogers, A soft, wearable microfluidic device for the capture, storage, and colorimetric sensing of sweat. *Sci. Transl. Med.* **8**, 366ra165 (2016).
23. R. C. Webb, Y. Ma, S. Krishnan, Y. Li, S. Yoon, X. Guo, X. Feng, Y. Shi, M. Seidel, N. H. Cho, J. Kurniawan, J. Ahad, N. Sheth, J. Kim, J. G. Taylor VI, T. Darlington, K. Chang, W. Huang, J. Ayers, A. Gruebele, R. M. Pielak, M. J. Slepian, Y. Huang, A. M. Gorbach, J. A. Rogers, Epidermal devices for noninvasive, precise, and continuous mapping of macrovascular and microvascular blood flow. *Sci Adv* **1**, e1500701 (2015).
24. R. C. Webb, S. Krishnan, J. A. Rogers, Ultrathin skin-like devices for precise, continuous thermal property mapping of human skin and soft tissues, in *Stretchable Bioelectronics for*

Medical Devices and Systems, J. A. Rogers, R. Ghaffari, D.-H. Kim, Eds. (Springer, 2016), pp. 117–132.
25. C. Zhu, A. Chortos, Y. Wang, R. Pfattner, T. Lei, A. C. Hinckley, I. Pochorovski, X. Yan, J. W.-F. To, J. Y. Oh, J. B.-H. Tok, Z. Bao, B. Murmann, Stretchable temperature-sensing circuits with strain suppression based on carbon nanotube transistors. *Nat. Electron.* **1**, 183–190 (2018).
26. T. Yokota, Y. Inoue, Y. Terakawa, J. Reeder, M. Kaltenbrunner, T. Ware, K. Yang, K. Mabuchi, T. Murakawa, M. Sekino, W. Voit, T. Sekitani, T. Someya, Ultraflexible, large-area, physiological temperature sensors for multipoint measurements. *Proc. Natl. Acad. Sci. U.S.A.* **112**, 14533–14538 (2015).
27. R. C. Webb, A. P. Bonifas, A. Behnaz, Y. H. Zhang, K. J. Yu, H. Y. Cheng, M. X. Shi, Z. G. Bian, Z. J. Liu, Y.-S. Kim, W.-H. Yeo, J. S. Park, J. Z. Song, Y. H. Li, Y. G. Huang, A. M. Gorbach, J. A. Rogers, Ultrathin conformal devices for precise and continuous thermal characterization of human skin. *Nat. Mater.* **12**, 938–944 (2013).
28. M. Hidaka, M. Matsumae, K. Ito, R. Tsugane, Y. Suzuki, Dynamic measurement of the flow rate in cerebrospinal fluid shunts in hydrocephalic patients. *Eur. J. Nucl. Med.* **28**, 888–893 (2001).
29. H. S. Carslaw, J. C. Jaeger, *Conduction of Heat in Solids* (Clarendon Press, ed. 2, 1959).
30. S. R. Madhvapathy, Y. Ma, M. Patel, S. Krishnan, C. Wei, Y. Li, S. Xu, X. Feng, Y. Huang, J. A. Rogers, Epidermal electronic systems for measuring the thermal properties of human skin at depths of up to several millimeters. *Adv. Funct. Mater.* **28**, 1802083 (2018).
31. R. C. Webb, R. M. Pielak, P. Bastien, J. Ayers, J. Niittynen, J. Kurniawan, M. Manco, A. Lin, N. H. Cho, V. Malyrchuk, G. Balooch, J. A. Rogers, Thermal transport characteristics of human skin measured in vivo using ultrathin conformal arrays of thermal sensors and actuators. *PLOS ONE* **10**, e0118131 (2015).
32. S. E. Gustafsson, Transient plane source techniques for thermal conductivity and thermal diffusivity measurements of solid materials. *Rev. Sci. Instrum.* **62**, 797–804 (1991).
33. S. Braley, The chemistry and properties of the medical-grade silicones. *J. Macromol. Sci. Chem.* **A4**, 529–544 (1970).
34. Nexperia Inc., 74HC4067; 74HCT4067: 16-channel multplexer/demultiplexer (Technical Data Sheet, 2015); https://assets.nexperia.com/documents/data-sheet/74HC_HCT4067.pdf.
35. J. F. Martínez-Lage, J. M. Martos-Tello, J. Ros-de-San Pedro, M. J. Almagro, Severe constipation: An under-appreciated cause of VP shunt malfunction: A case-based update. *Childs Nerv. Syst.* **24**, 431–435 (2008).
36. V. V. Ragavan, M. Swoboda, C. Laing, S. C. Stein, Evaluation of shunt flow through a hydrocephalic shunt: A controlled model for evaluation of the performance using Shuntcheck (NEURODX Development, 2017); http://neurodx.com/wp-content/uploads/2017/10/Stein-2008-Evaluation-of-Shunt-Flow-Through-a-Hydrocephalic-Shunt-A-Contrilled-Model-of-Evaluation-of-the-Performance-Using-ShuntCheck.pdf.

Acknowledgments: T.R.R. acknowledges C. Andreou for discussions regarding PCA analysis. **Funding:** We would like to acknowledge funding support provided by the Center for Bio-Integrated Electronics at Northwestern University and by the Dixon Translational Research Grants at Northwestern University. Y.M. and X.F. acknowledge the support from the National Basic Research Program of China (grant no. 2015CB351900) and the National Natural Science Foundation of China (grant nos. 11402135 and 11320101001). Y.H. acknowledges the support from the NSF (grant nos. 1400169, 1534120, and 1635443). K.L. acknowledges funding support from the Samsung Fellowship. This work used Northwestern University Micro/Nano Fabrication Facility (NUFAB), which is partially supported by the Soft and Hybrid Nanotechnology Experimental (SHyNE) Resource (NSF ECCS-1542205), the Materials Research Science and Engineering Center (NSF DMR-1720139), the State of Illinois, and Northwestern University. **Author contributions:** S.R.K., T.R.R., A.B.A., and J.A.R. led the development of the concepts, designed the experiments, interpreted the results, and wrote the paper. S.R.K. and T.R.R. led the experimental work with support from P.G., K.L., J.Y.L., B.N., J.S., N.K., G.Y., I.S., J.F., C.G., and J.C. Y.M., C.W., X.F., and Y.H. performed the thermal modeling and simulations. A.B.A., M.T., and M.P. led the design and development of the patient trials and were assisted by Z.A.A. and N.M. All authors contributed to proofreading the manuscript. **Competing interests:** S.R.K., A.B.A., T.R.R., P.G., and J.A.R. are inventors on patents and patent applications related to thermal sensing, including applications in hydrocephalus diagnostics. S.R.K., T.R.R., A.B.A., M.P., and J.A.R. are cofounders of Rhaeos Inc., a company that develops wireless, wearable shunt diagnostic sensors. The devices described here are similar to devices that will be featured in the company's portfolio. J.A.R. has also founded multiple companies related to biosensors, including Epicore Biosystems, Wearifi Inc., NeuroLux Inc., and others. S.R.K. is engaged part-time by NeuroLux Inc., a company that develops wireless neuroscience tools, and P.G. serves as an unpaid consultant for the same company. J.C. is a cofounder and chief technological officer of J2 Materials, a company that produces diamond for the semiconductor industry. **Data and materials availability:** All data needed to evaluate the conclusions are present in the paper or in the Supplementary Materials. All information and materials can be requested from one of the corresponding authors.

Submitted 10 April 2018
Accepted 11 October 2018
Published 31 October 2018
10.1126/scitranslmed.aat8437

Citation: S. R. Krishnan, T. R. Ray, A. B. Ayer, Y. Ma, P. Gutruf, K. Lee, J. Y. Lee, C. Wei, X. Feng, B. Ng, Z. A. Abecassis, N. Murthy, I. Stankiewicz, J. Freudman, J. Stillman, N. Kim, G. Young, C. Goudeseune, J. Ciraldo, M. Tate, Y. Huang, M. Potts, J. A. Rogers, Epidermal electronics for noninvasive, wireless, quantitative assessment of ventricular shunt function in patients with hydrocephalus. *Sci. Transl. Med.* **10**, eaat8437 (2018).

Science Translational Medicine

Epidermal electronics for noninvasive, wireless, quantitative assessment of ventricular shunt function in patients with hydrocephalus

Siddharth R. Krishnan, Tyler R. Ray, Amit B. Ayer, Yinji Ma, Philipp Gutruf, KunHyuck Lee, Jong Yoon Lee, Chen Wei, Xue Feng, Barry Ng, Zachary A. Abecassis, Nikhil Murthy, Izabela Stankiewicz, Juliet Freudman, Julia Stillman, Natalie Kim, Grace Young, Camille Goudeseune, John Ciraldo, Matthew Tate, Yonggang Huang, Matthew Potts and John A. Rogers

Sci Transl Med **10**, eaat8437.
DOI: 10.1126/scitranslmed.aat8437

Sensors for shunts

Ventricular catheters (shunts) relieve pressure on the brain by rerouting excess cerebrospinal fluid that accumulates in patients with hydrocephalus. Catheter occlusion or malfunction can be difficult to diagnose without medical imaging or surgery. Here, Krishnan *et al*. fabricated thin, flexible, epidermally adherent sensors to monitor subdermal shunt function. In five subjects with hydrocephalus, the sensors could detect direction-dependent heat transport associated with fluid flow at skin sites over the catheter versus skin adjacent to the catheter. The sensors detected shunt malfunctions in some patients that were confirmed by imaging or surgery. With wireless data transfer capabilities, these flexible sensors offer a noninvasive way to monitor shunt function.

Science Translational Medicine
AAAS

www.sciencetranslationalmedicine.org/cgi/content/full/10/465/eaat8437/DC1

Supplementary Materials for

Epidermal electronics for noninvasive, wireless, quantitative assessment of ventricular shunt function in patients with hydrocephalus

Siddharth R. Krishnan, Tyler R. Ray, Amit B. Ayer, Yinji Ma, Philipp Gutruf, KunHyuck Lee, Jong Yoon Lee, Chen Wei, Xue Feng, Barry Ng, Zachary A. Abecassis, Nikhil Murthy, Izabela Stankiewicz, Juliet Freudman, Julia Stillman, Natalie Kim, Grace Young, Camille Goudeseune, John Ciraldo, Matthew Tate, Yonggang Huang, Matthew Potts*, John A. Rogers*

*Corresponding author. Email: matthew.potts@nm.org (M.P.); jrogers@northwestern.edu (J.A.R.)

Published 31 October 2018, *Sci. Transl. Med.* **10**, eaat8437 (2018)
DOI: 10.1126/scitranslmed.aat8437

The PDF file includes:

Other Supplementary Material for this manuscript includes the following:

(available at www.sciencetranslationalmedicine.org/cgi/content/full/10/465/eaat8437/DC1)

Movie S1 (.mp4 format). Wireless ELA pairing to smartphone app and on-demand actuation.
Movie S2 (.mp4 format). Experimental system in movie S1.

Materials and Methods

Sensor construction

The Epidermal Square Array (ESA) comprised a circular (R = 2.5 mm) thin-film metallic (Cr/Au 10/50 nm) actuating element surrounded by 100 circular (R = 0.25 mm) thin-film metallic (Cr/Au 10/50 nm) temperature sensors while the Epidermal Linear Array (ELA) had an identical actuating element, but with 4 temperature sensors. For the ESA, two layers of metallic traces (Ti/Cu/Ti/Au 20/600/20/25 nm) patterned in serpentine geometries defined interconnects between the sensing and actuating elements, with polyimide (PI) as an interlayer dielectric. For the ELA, a single thin-film metallization layer (Cr/Ai, 10/100 nm) was the basis for the actuator, the sensors and the serpentine interconnects. For both designs, a film of PI (9 μm total thickness) patterned and aligned to the metal features served as an encapsulation layer and a soft (70 kPa) elastomeric substrate (100 μm) served as a support for the ultrathin electronics.

Fabrication began with spin-casting a sacrificial layer of poly(methyl methacrylate) (700 nm) onto a 4", undoped Si-wafer. A dielectric layer, polyimide (PI, 3 μm) was then spun on. For the epidermal linear array (ELA), a single bilayer film of Cr/Au 10/100 nm was deposited by electron-beam evaporation onto the wafer, and patterned by photolithography and etching formed the sensors and serpentine interconnects, in accordance with design rules in stretchable electronics (*40-43*). For the epidermal square array (ESA), a bilayer film of Cr/Au 10/100 nm was photolithographically defined to form 100 resistive temperature sensing elements, arranged in a 10 x 10 array, around a central resistive thermal actuator. Successive metallization and photolithography defined input and output lines to address each sensor, and a final dielectric layer of PI, spin cast and defined via photolithography and plasma-etching encapsulated the entire device. For both the ELA and ESA designs, spin-casting defined a final layer of PI layer (3 μm) also patterned in the geometry of the metal traces. A final reactive ion etching (RIE) step isolated the outline of the device and opened via holes for wired connections to external data acquisition electronics. Immersion in an acetone bath undercuts the sacrificial PMMA layer, allowing for release and transfer via water soluble tape (Aquasol Inc)4. The devices were then transferred to a thin, bi-layer silicone membrane (Ecoflex, 20 μm, Dow Corning, MG 7 1010 Skin Adhesive, 20 μm), spin-cast onto a glass slide. Immersion in warm water dissolved the tape, and a spin-cast top layer of silicone (Ecoflex, 50 μm) completed the device. A thin (100 μm), double-sided sheet adhesive (JMS 1400, Label Innovations) was laser structured to form an outline around the

device. This sheet adhered to the silicone and a handling frame, either in the form of a printed circuit board containing wireless transmission electronics, or a simple, thick, elastomeric frame to facilitate handling of the wired electronics. Anisotropically conducting films (ACF) established connections to wired data acquisition electronics. The sensor resistances were then calibrated to temperatures measured by IR imaging. Detailed fabrication steps are below.

Fabrication of the epidermal square array (ESA)

A. Wafer preparation

1. Spin coat PMMA onto clean, dry silicon wafer and bake at 180°C for 3 minutes
2. Spin cast Polyimide (PI 2545) at 3000 rpm for 30 s (3 μm film)
3. Cure at 90°C for 30 s, 150°C for 5 minutes, and 250°C for 1 hr and 10 mins under vacuum and N2 purge (PI oven is recommended)

B. First metallization layer

4. Deposit Cr/Au bilayer, 10/50 nm, by e-beam evaporation (or by sputtering if sources are available) (Sensor resistance: 250 Ohm, heater resistance: 24 kOhms.)

5. Spin coat AZ 5214 PR, at 3000 rpm for 30 s

6. Bake at 110 °C for 60 s

7. Expose with 365 nm (i-line) and through appropriate mask (exposure energy 54 mJ, 6 s on MA6 Ch1)

8. Develop in AZ 400K (4:1 Water:Developer) for 50 s. Undiluted AZ917 MIF will also work.

9. Etch away gold (KOH+KI solution) and Cr layers.

10. Wash off photoresist

C. Second metallization layer

11. Deposit Ti/Cu/Ti/Cu 30 nm/550 nm/30 nm/50 nm by ebeam evaporation

12. Spin coat AZ 5214 PR, at 3000 rpm for 30 s

13. Bake at 110 ˚C for 60 s

14. Expose through appropriate mask (exposure energy 54 mJ, 6 s on MA6 Ch1)

15. Develop in AZ 400K (4:1 Water:Developer). Undiluted AZ917 MIF will also work.

16. Etch away metal layers (Titanium etches in BOE, traditional etchants for the rest).

17. Wash off photoresist

D. PI dielectric layer

18. Spin PI 2545, 6000 rpm for 30 s

19. Cure for 30s at 90 ˚C, 5 mins at 150, 1 hr 10 mins at 250 ˚C under vacuum and N2 purge (PI oven is recommended)

20. Repeat step 20-21 (double layer is to prevent pinholes in PI film)

21. Spin SPR 220 PR, 3000 rpm, 30 s

22. Bake at 110 ˚C for 180 s

23. Expose with 365 nm light (i-line) and appropriate mask (should be clear polarity). Total exposure energy = 117 mJ (13s on MA6)

24. Develop in AZ 400K 4:1 for 90 s

25. Etch in March RIE: 25 SCCM O2, 200 mTorr, 200W, 800s. If unsure, probe after 600 s. Remove remaining PR via flood exposure and development in undiluted AZ 400K.

E. Third metallization layer

26. Deposit Ti/Cu/Ti/Cu 30nm/550nm/30nm/50nm by ebeam evaporation

27. Spin SPR 220 PR, 3000 rpm, 30 s

28. Bake at 90 ˚C for 180 s

29. Expose with 365 nm light (i-line) and appropriate mask. Total exposure energy = 117 mJ (13 s on MA6)

30. Develop with AZ 400K 4:1, for 120 s

31. Etch metal layers

32. Wash off PR

F. Final PI layer

33. Spin cast Polyimide (PI 2545) at 3000 rpm for 30 s (3 μm film).

34. Cure at 90 ˚C for 30 s, 150 ˚C for 5 minutes and 250 ˚C for 1hr 10 mins under vacuum and N2 purge (PI oven is recommended)

35. Deposit 75 nm SiO_2 via sputtering

36. Spin AZ 5214, 30s, 2000rpm, bake for 30s

37. Expose through appropriate mask 10s, develop in AZ400K, 4:1

38. Etch using SF6 chemistry in RIE

39. RIE etch using the following parameters: 13.3 Pa, 200W, 100 SCCM O2 70 minutes

G. Release and transfer

40. Release in room temperature acetone for 6 hrs

41. Transfer using water soluble tape (PVA or cellulose)

42. Deposit 75 nm SiO_2 onto devices mounted on tape via sputtering

43. Separately, prepare surface treated glass slides (preferably treated with PMMA), with ecoflex spun at 3000 rpm

44. Place glass slides in UVO box for 5 mins or corona treater for 30 s

45. Immediately transfer devices with SiO_2 face down onto hydrophilic ecoflex.

46. Cure at 70 ˚C for 1hr

47. Dissolve tape in warm water for 90 minutes

48. Dry overnight and make external connections

Fabrication of epidermal linear arrays (ELA)

A. Wafer preparation

1. Spin coat PMMA onto clean, dry Silicon wafer and bake at 180˚C for 3 minutes
2. Spin cast Polyimide (PI 2545) at 3000 rpm for 30s (3 μm film).
3. Cure at 90 ˚C for 30 s, 150 ˚C for 5 minutes and 250 ˚C for 1hr 10 mins under vacuum and N2 purge (PI oven is recommended)

B. First metallization l**ayer**

4. Deposit Cr/Au bilayer, 10/50 nm, by e-beam evaporation (Sensor resistance- 250 Ohm, heater resistance- 24 kOhms.)

5. Spin coat AZ 5214 PR, at 3000 rpm for 30 s

6. Bake at 110 ˚C for 60 s

7.. Expose with 365 nm (i-line) and through appropriate mask (exposure energy 54 mJ, 6 s on MA6 Ch1)

8. Develop in AZ 400K (4:1 Water:Developer) for 50 s. Undiluted AZ917 MIF will also work.

9. Etch away gold (KOH+KI solution) and Cr layers.

10. Wash off photoresist

C. Final PI layer

11. Spin cast Polyimide (PI 2545) at 3000 rpm for 30 s (3 μm film).

12. Cure at 90 ˚C for 30 s, 150 ˚C for 5 minutes and 250 ˚C for 1hr 10 mins under vacuum and N2 purge (PI oven is recommended)

13. Deposit 75 nm SiO_2 via sputtering

14. Spin AZ 5214, 30 s, 2000 rpm, bake for 30 s

15. Expose through appropriate mask 10 s, develop in AZ400K, 4:1

16. Etch using SF6 chemistry in RIE

17. RIE etch using the following parameters: 13.3 Pa, 200 W, 100 SCCM O2 70 minutes

D. Release and transfer

18. Release in room temperature acetone for 6 hrs

19. Transfer using water soluble tape (PVA or cellulose)

20. Deposit 75 nm SiO_2 onto devices mounted on tape via sputtering

21. Separately, prepare surface treated glass slides (preferably treated with PMMA), with ecoflex spun at 3000 rpm

22. Place glass slides in UVO box for 5 mins or corona treater for 30 s

23. Immediately transfer devices with SiO_2 face down onto hydrophilic ecoflex.

24. Cure at 70 ˚C for 1 hr

25. Dissolve tape in warm water for 90 minutes

26. Dry overnight and make external connections

Fabrication of flexible printed circuit boards

Fabrication began with a commercially available, dense, tri-layer Cu/PI/Cu laminate (Pyralux, 6535, DuPont, 18 μm/75 μm/18 μm). Laser structuring (LPKF U4, LPKF Systems) patterned conducting traces and bond pads, with a resolution of 50 μm. Reflow soldering established electronic connections to commercially available SMD resistors and capacitors, along with a Bluetooth microcontroller (NRF 52, Nordic Semiconductor).

Data acquisition systems

Data were recorded from the ELA resistive elements via digital multimeters (DMM) (NI, USB 4065, National Instruments). A constant current source supplied actuation power (Keithley 6220, Tektronix). A schematic

of this system appears in fig. S2. The ESA requires a voltage output module (NI 9264, National Instruments) that sequentially actuates each of the ten input channels with 3V, and a single- channel DMM to measure current. A red LED connected in series with each channel serves as a visual indicator of multiplexing and the status of each addressed channel. A mechanical reed relay module (J-Works, 2418, J-Works Inc.) enabled time multiplexed measurements from each of the ten channels. All data were recorded via custom software designed and programmed in LabView (National Instruments), and processed with custom algorithms in Matlab (Mathworks Inc.). A schematic of this system appears in Fig S2. For the wireless embodiment a commercially available Bluetooth chip (NRF 52832, Nordic Semiconductor) performed all on-board control, data acquisition and transmission using a custom firmware. was performed controlled by custom firmware wirelessly transmitted data to a smartphone (Samsung Galaxy S6) where a custom mobile application logged and displayed data.

Benchtop experiments

We constructed a phantom skin assembly for in vitro flow evaluation, with a distal shunt catheter (Medtronic, Minneapolis, MN, OD = 1.5 mm, ID = 0.75 mm) embedded in a matrix of PDMS (Sylgard 184, Dow Corning) supported by a 3D-printed mold. Optical images of this assembly appear in fig. S6, revealing h_{skin} = 1.1 mm. A calibrated syringe pump (Harvard Apparatus) controlled the flow rate of water. The syringe pump reached a steady state at a flow rate for 180s before each recorded measurement. Each measurement consisted of a 60s "off" period with $Q_{actuator}$<0.001 mW/mm^2, followed by a 600s actuation ("on") period, with $Q_{actuator}$ = 1.45 mW/mm^2, followed by a 180s off period to return the sensor back to its baseline, pre-actuation temperature value. Simultaneously, IR images were recorded with an IR camera (FLIR Systems, a6255sc), with a high-magnification lens. Casting PDMS onto 3D printed molds with negative relief structures with defined heights yielded different phantom skin thicknesses that were used for the testing described above.

ESA temperature map generation

Precise temperature measurements involved recording changes in resistance of each sensor in the ESA and converting the results to temperatures via a linear calibration (goodness of fit, fig. S3). Voltage (V_{sup}, 3V) and current (I_{meas}) were sequentially applied to, and measured from, each of the 10 rows and columns in the array, respectively. For any given element in the array, the combination of a known supply voltage and measured current allows for the precise calculation of resistance and, therefore, temperature. A custom MATLAB program generated a 2D array (10 x 10) of background-subtracted temperatures from these data for each measurement in a time-series

recording. The known spatial coordinates of each sensor element facilitated transformation into a sparse square mesh array (170 x 170) of temperature pixels representing the physical ESA surface (17 x 17 mm; 10 px mm^{-1}). A bicubic interpolation algorithm (*44*) populated the spatial array with interpolated temperature values that yielded the ESA spatial temperature map. Subsequent subtraction of the heater-on, no-flow steady state temperatures from all time sequence measurement points enhanced the visualization of flow-induced thermal anisotropy.

Spatial interpolation for heat maps

The density of the ESA enables spatial mapping of the temperature anisotropy that results from fluid flow. These maps result from the processing of raw measurements from the ESA. The ESA is represented by a 10 x 10 x N tensor (variables noted in bold are matrices), where the rows and columns map to sensor position (fig. S6A) and N is the total number of frames (time points) in an ESA measurement sequence. A linear calibration curve for each sensor enabled direct conversion of the raw ESA measurements ($\mathbf{I_{meas}}$, converted to resistance via V = IR), to temperature (fig. S6B). As previously described, the ESA, placed on a hotplate, recorded a series of steady-state temperatures (n = 5+) for fixed time intervals (5 min) while time-series IR thermographs simultaneously record the temperatures of the hot plate and ESA. A linear least squares fit provided a linear calibration between the temperature values recorded via IR thermography and the measurements recorded for each ESA sensor yielding a $\mathbf{T_{cal}}$ calibration matrix (10 x 10). Converting the raw ESA measurements with $\mathbf{T_{cal}}$ yields $\mathbf{T_{ESA,\ N}}$ which is the calibrated ESA temperature measurements at time N (fig. S6B). $\mathbf{T_{ESA,\ N}}$ was the basis for all subsequent ESA data processing.

Conversion of $\mathbf{T_{ESA,\ N}}$ to $\mathbf{T_{NORMALIZED,\ N}}$ results from the subtraction of the background temperature $\mathbf{T_{BACKGROUND}}$ from each frame N (fig. S6C). This background subtraction eliminates the temperature signal beyond the signal generated by the thermal actuator. This results in the boundary conditions (the background subtracted on-skin temperature) for $\mathbf{T_{NORMALIZED,\ N}}$ being 0 °C, as verified from IR thermography. As the signal relevant to the analysis and visualization of flow is the flow-induced anisotropic thermal transport, the isotropic heat transfer component from the thermal actuator $\mathbf{T_{ACTUATOR}}$ (signal without flow) is subtracted from each frame N. $\mathbf{T_{ACTUATOR}}$ is assumed to be a constant value for a given on-body test as it directly depends on the thermal transport

characteristics of the skin of a patient. Practically, this requires a short (~ 1 min) ESA measurement of the steady-state isotropic heat transport resulting from the thermal actuator at an off-catheter location on the patient's body.

The density of the ESA enables the mapping of temperature values to the physical spatial coordinates of each sensor to generate an epidermal analog to IR thermography. As the physical locations of each sensor, with respect to the thermal actuator (centered at 0 mm, 0 mm), are known *a priori*, a sparsely populated square matrix corresponding to physical device dimensions provides a virtual device representation where each matrix value (i^{th} row, j^{th} column) is a simulated square thermal "pixel." For this work, a simulated square "pixel" array is larger than the ESA (physical grid:17 mm x 17 mm, 10 px mm^{-1}) resulting 170 x 170 x N tensor of a time-series measurement of N frames. The values from $\mathbf{T_{NORMALIZED,\ N}}$ are then mapped to the sensor locations contained in the pixel array. The temperature map results from fitting a surface to the measured $\mathbf{T_{NORMALIZED,\ N}}$ values for each frame N via meshed bicubic interpolation in MATLAB (*44*) (boundary conditions °C from IR thermograph, thermal actuator temperature recorded during ESA measurement), the results shown in fig. S6D. As this is a sparsely populated matrix, the interpolation process fits a surface of best fit to capture the included data points with a weighting preference given to fitting the data rather than yielding a smooth surface fit — an approach commonly found in cartography for mapping contoured topography data (*45*) and medicine for brain imaging (*46*).

As the signal relevant to the analysis and visualization of flow is the flow-induced anisotropic thermal transport, the isotropic heat transfer component from the thermal actuator $\mathbf{T_{ACTUATOR}}$ (signal without flow) is subtracted from each frame N (with actuator activated). $\mathbf{T_{ACTUATOR}}$ is assumed to be a constant value for a given on-body test as it directly depends on the thermal transport characteristics of the skin of a patient. Practically, this requires a short (~ 1 min) ESA measurement of the steady-state isotropic heat transport resulting from the thermal actuator at an off-catheter location on the patient's body.

Principle components analysis (PCA)

The schematic illustration in fig. S4A identifies two regions of the ESA (upstream, downstream) which each contain a set of 50 temperature sensors. fig. S4B shows a PCA analysis of an additional flow study to that presented in Fig. 2 of the main text to illustrate the utility in distinguishing between actuator state (heat on/off) and flow condition (no flow, flow) for ESA sensors both inline and normal to the catheter position. The study used a

single flow condition of 0.02 ml/min and an actuation power of 1.8 mW mm^{-2}. As fig. S5B indicates, the flow state is distinguishable via PCA analysis regardless of sensor alignment (inline *vs.* normal).

A series of PCA models for different upstream sensors (identified via color in fig. S5A) were generated to better explore the utility of Principle Component Analysis (PCA) in identifying orientation of the ESA to the catheter (and thus flow) shown in fig. S6C. The flow data is the same as presented in Fig. 2 containing two different flow states (0.02 ml/min and 0.2 ml/min). As stated previously, the first two components (PC1, PC2) describe approximately 92% of the overall variability of the data (~70.5% PC1, ~22.1% PC2) with the remainder (8% across PC3:PC50) associated with noise. A comparison of the data clusters and principal components shows that PC1 primarily relates to the degree of thermal actuation while PC2 relates to the presence or absence of flow. Mapping the variables to the PCA biplot indicates sensor correlation to fluid flow. In each PCA biplot, an overlay of largest factor corresponding to the downstream sensor known to be proximal (red) to fluid flow shows the positive correlation to fluid flow for both orthogonal and inline upstream sensors (fig. S6C). Fig. S6C shows PCA models for each sensor (1-5). As the selected sensor approaches the inline orientation (aligned), the separation between flow off / flow on clusters increase in magnitude. When aligned with the flow, the orientation PCA model components PC1 and PC2 most strongly reflect thermal actuation and flow state (fig. S5C). This further supports the utility of PCA for scenarios without *a priori* orientation in evaluating correlations between upstream sensors and flow state and, therefore, orientation of the catheter relative to the ESA. With ESA orientation established, a separate PCA model for the actual thermal flow data ($\mathbf{T_{NORMALIZED,\,N}}$) provides direct classification of thermal actuation state and flow state whereby the PC1 correlates with flow (positive is flow) and PC2 correlates with thermal actuation state as shown in fig. S6C-Data.

Transient plane source for in-vivo measurements of thermal transport

Measurement of thermal transport properties in-vivo is accomplished via curve fitting the transient temperature rise of the circular actuator, $T_{actuator}$ after low power actuation begins. This rise is given by

$$\overline{\Delta T_{actuator}(\tau)} = P_{actuator}\left(\pi^{\frac{3}{2}}ak\right)^{-1} D(\tau) \qquad (1)$$

Where $P_{actuator}$ is the total power supplied ($P=I^2R$), and $D(\tau)$ is given by

$$D(\tau) = \int_0^{\tau} d\sigma\sigma^{-2} \int_0^1 udu \int_0^1 vdv \times \exp\left(\frac{-(u^2+v^2)}{4\sigma^2}\right) I_0\left(\frac{uv}{2\sigma^2}\right) \qquad (2)$$

Where τ is dimensionless time, given by

$$\tau = \sqrt{t\alpha/a^2} \quad (3)$$

The thermal properties of interest, thermal conductivity (k) and diffusivity (α) can therefore be fitted from the analytical equations above. The quantity a represents a characteristic length associated with the sensor diameter. Calibration of the sensor with test media bounding the thermal properties of skin (Water, Ethylene Glycol) yield an effective value of a that accounts for sensor's multilayered construction and coiled geometry. Time-dependent diffusion defined the penetration depth of these sensors and is computed numerically revealing most of the thermal field to be confined to <1.5 mm after 4s of actuation, as shown in fig. S7.

In vivo measurements of thermal properties and flow

Transient, off-shunt measurements of $T_{actuator}$ define the thermal transport properties of the patient's skin. A representative response before, during and after actuation appear in Fig. 5D. Fitting data collected over relatively short actuation times (4s) allows determination of thermal properties associated with the superficial, avascular epidermal skin layers relevant for the flow measurements. Values of k_{skin} and α_{skin} extracted from these data appear in Figs. 5E-F; the magnitudes are comparable to expected values. Data from the flow sensor are in figs. S25 C-D, where the red, black and blue curves represent the temperatures measured from the upstream sensor, the downstream sensor, and the actuator, respectively.

Locations adjacent to the shunt that are free of near-surface blood macrovessels present no sources of thermal anisotropy and, therefore, can serve as control measurements. Results from a representative case are in fig. S26, where the upstream and downstream responses are nearly identical.

Effect of near-surface blood flow

A possible confounding effect for the measurement follows from blood flow through superficial veins, as shown in a benchtop model in fig S21 for two skin thicknesses and in two configurations: flow aligned with (+x, co-flow) and opposite to (-x, counter-flow) flow of CSF flow, for rates at the upper end of the range typically encountered in veins located near the surface of the skin of the neck (*28*). In practice, co-flow represents the most realistic case, as venous blood flow typically proceeds from the brain towards the heart. Arterial flow can be

neglected since its depth (>1 cm) occurs below the limit of detectability for the sensors reported here. In experiments, flow through the catheter is 0.13 ml/min, and the phantom blood vessel (R_{vessel} = 1 mm) resides (d_{blood}) 5 mm from the central axis of the ELA, and 2.5 mm from the edge of the actuator, as an extreme case. In this system, h_{skin} is the same for both the catheter and the blood vessels. The counter-flow cases result in a 20% reduction in both $\Delta T_{sensors}/ T_{actuator}$ and $\overline{T}_{sensors}/T_{actuator}$, while the co-flow case results in a measured reduction of <5%, corresponding to an overestimation of flow by 20% and 5% respectively. In practice, the ELA can easily be placed to avoid near-surface blood macro-vessels using a hand-held vein mapping tool (*28*).

DAQ noise

Data analysis requires conversion of measured resistances from two sensors and one actuator into temperatures, and then into a flow rate. The first conversion relies on a precise, high-resolution (10 mΩ) measurement of resistance performed with a digital multimeter (fig. S17A) at a sampling frequency of 5 Hz. The inherent noise in the resistance measurement is 4.8 ppm over a 20-minute sampling window, as measured with a commercial, 1kΩ resistor and shown in fig. S17B. The addition of a conducting anisotropic thin film (ACF) cable increases the noise to 12.5 ppm. Introducing the soft temperature sensing element and a second ACF connection further increases the noise to 93.9 ppm. Conversion to temperature relies on a linear calibration with R^2>0.999, corresponding to a temperature resolution of 15 mK. Actuation involves a high-performance constant current source that exhibits remarkably stable operation, with deviations of 1.73 ppm over a 20-minute sampling window, as shown in fig. S17C.

Power spectral density calculations showing primarily low-frequency 1/f noise appear in fig. S17E. Artifacts associated with high-frequency noise, as measured with an oscilloscope appear in fig. S18. Fourier transforming data over a 50 μs sampling window reveals primarily low-frequency noise and a peak at 50/60 Hz, as shown in fig. S18B. Effects associated with shot-noise are revealed in these high frequency measurements. Multiple (n = 5) successive resistance measurements over narrow sampling windows and times (n = 10-10000, t =1-1000 ns) revealed regimes where computed signal to noise (SNR = $R_{avg\ n=5}/\sigma_{n=5}$) scales linearly with the $\sqrt{N}$ as shown in figs. S18 C-D.

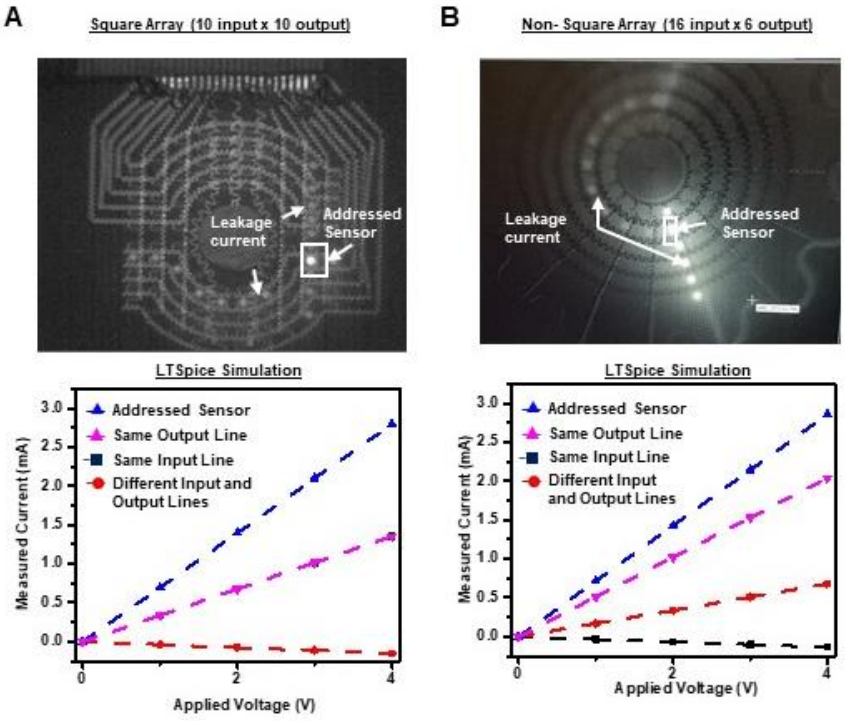

Fig. S1. Current pathways through resistive arrays. (A) IR image (top) and LTSpice current simulations of ESA (bottom), with equal number of input (V_{sup}) and output (I_{meas}) lines, with single sensor addressed with V_{sup} = 0.5V showing currents through same input line (row) and output line (column), illustrating current leakage pathways. **(B)** Same as (A) but for a non-square array (16 x 6), showing large power dissipation through non-addressed sensors in same output line (spoke).

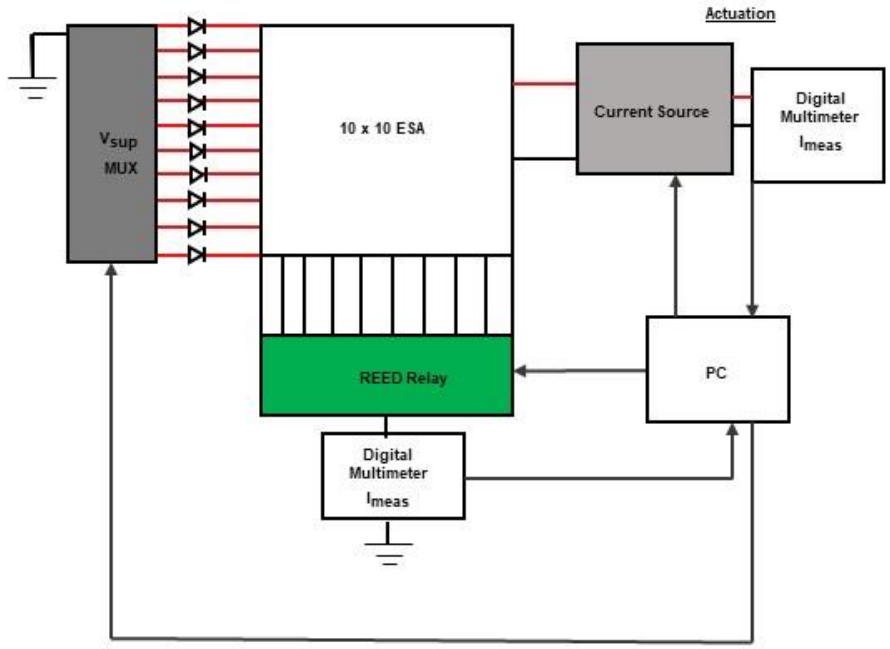

Fig. S2. Schematic illustration of the DAQ and control system for an array of 100 sensors. Schematic shows mechanical switching modules for rapid multiplexed addressing, digital multimeters for resistive temperature measurements and a constant-current source for controlled, low-power dc thermal actuation.

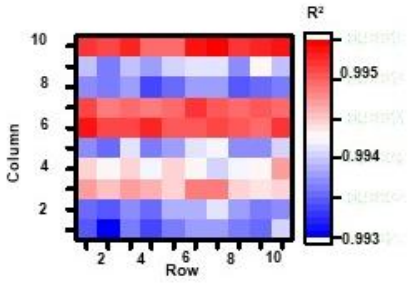

Fig. S3. Calibration map for ESA. Temperature distribution, where each pixel corresponds to a residual (R^2) value computed for each element in a 10 x 10 array from linearly fitting I_{meas} to temperature for calibration, along with flow chart detailing processing algorithm, with R^2 >0.99 across the array.

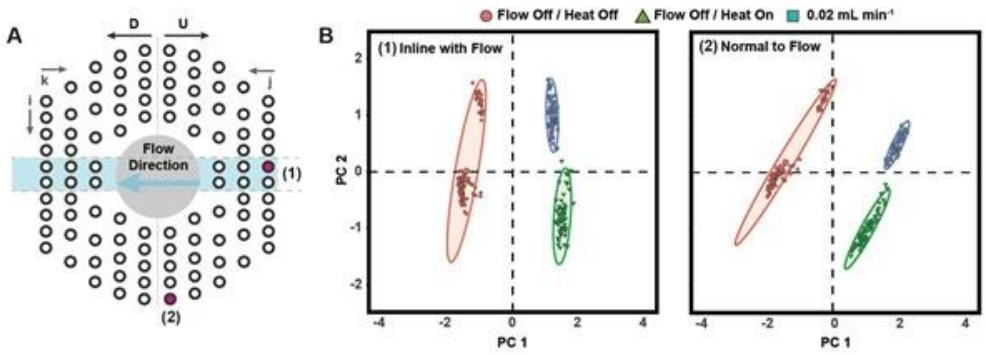

Fig. S4. PCA for determining the presence of flow with an ESA. (A) Spatially precise schematic map of a device with 100 sensors, with tube position overlay and upstream (U) and downstream (D) temperatures. **(B)** Principal components analysis (PCA) biplot (principle component 1 and 2) of baseline-subtracted differentials for two conditions: a U sensor known to be (1) inline and (2) normal to the underlaid catheter in a benchtop system. For each condition, the selected U sensor and each D sensor comprise the baseline-subtracted differentials. Clustering occurs for the following cases: no flow and no actuation; no flow with actuation at 1.8 mW/mm^{-2}; Actuation at 1.8 mW mm^{-2} and flow at 0.02 ml/min.

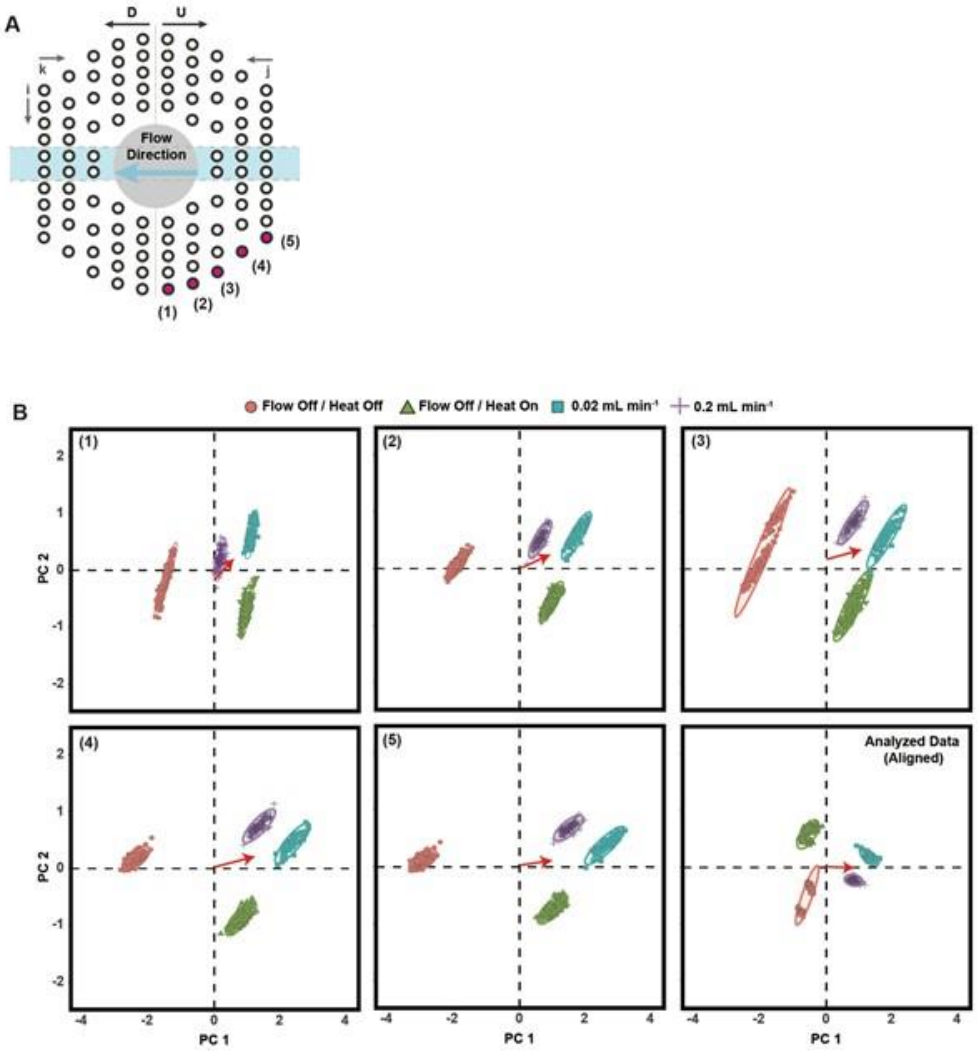

Fig. S5. PCA for determining the orientation and magnitude of flow with an ESA. (A) Spatially precise schematic map of a device with 100 sensors, with tube position overlay and upstream (U) and downstream (D) temperatures. **(B)** Principal components analysis (PCA) biplot (principle component 1 and 2) of baseline-subtracted differentials between five (1-5) selected U sensors and each D sensor-illustrating the identification of the sensors aligned with the flow direction regardless of selected sensor (red vector). When a PCA model is applied to the aligned data (used to generate temperature maps in Fig. 2E). PC1 correlates to presence / absence of flow and PC2 corresponds to thermal actuation state (on / off).

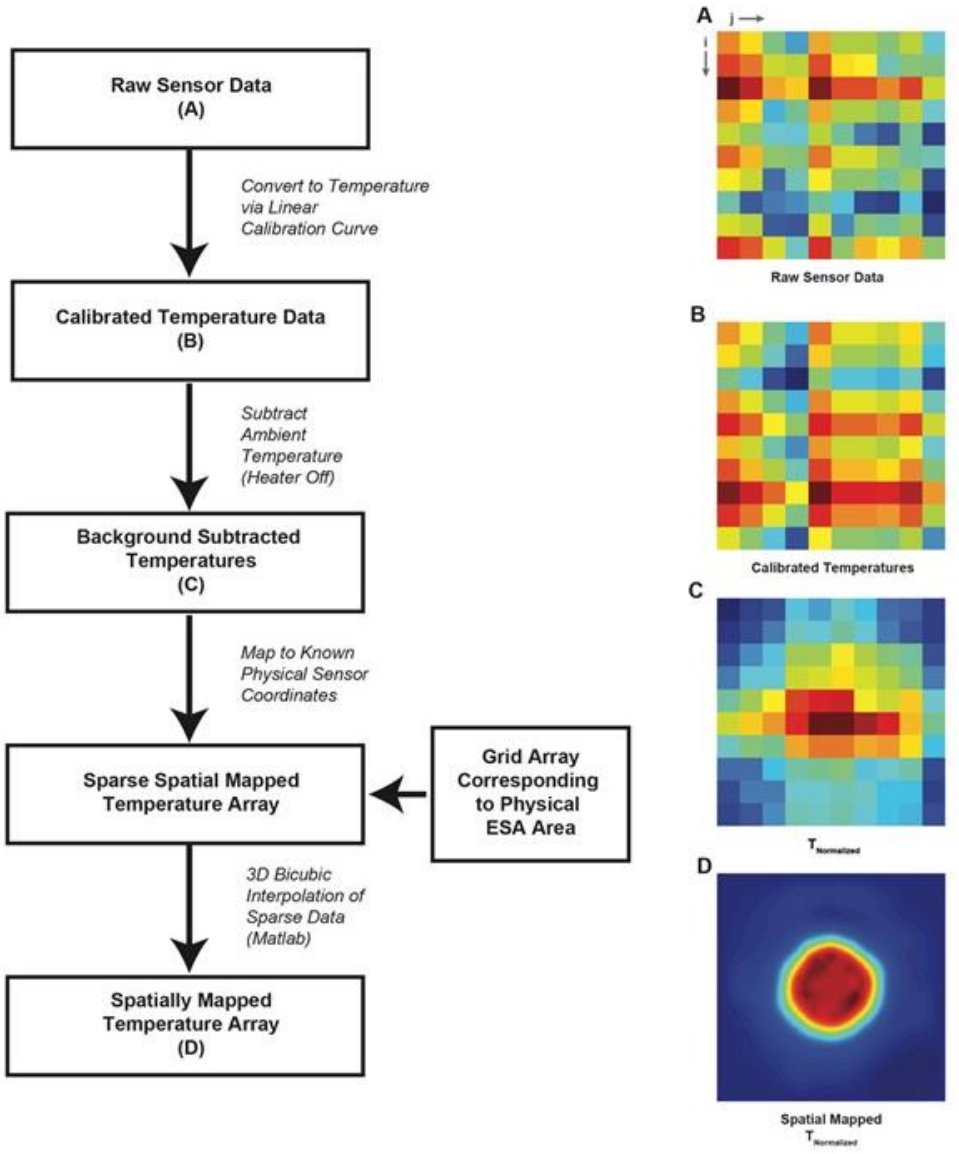

Fig. S6. Flow diagram detailing the process for conversion of raw ESA sensor recordings to a spatial temperature map. (A). Example of raw ESA data. **(B)** Transformation of raw ESA data to temperature via a calibration curve specific to each ESA. **(C)** Temperature differentials resulting from the removal of background temperature **(D)** ESA temperature map obtained from C by meshed bicubic interpolation of the sparsely populated grid array. This grid array corresponds to the physical dimensions of the ESA.

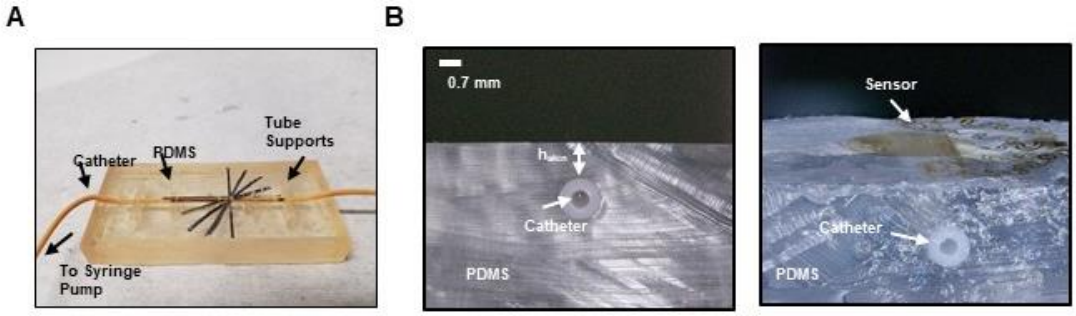

Fig. S7. Benchtop flow system. (A) Optical image of a benchtop system for studying responses to flow through an embedded shunt based on silicone skin phantom with tunable thickness. **(B)** Optical micrographs in cross section and isometric views showing the catheter geometry and h_{skin}.

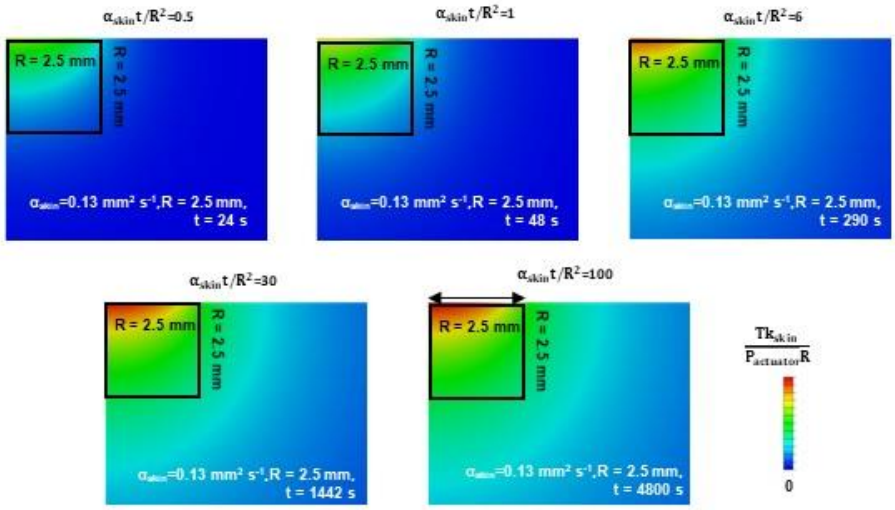

Fig. S8. Depth of thermal penetration. Dimensionless scaling parameters illustrating the time evolution of heat through the skin, as a measure of depth penetration, with experimentally measured values for time (24s, 48s, 290s, 1442s, 4800s), thermal conductivity (k_{skin} = 0.35 W $m^{-1}K^{-1}$) , thermal diffusivity (α_{skin} = 0.13 mm^2s^{-1}) and actuator size ($R_{actuator}$ = 2.5 mm). Dimensionless analysis is chosen to allow for facile tuning of key system parameters.

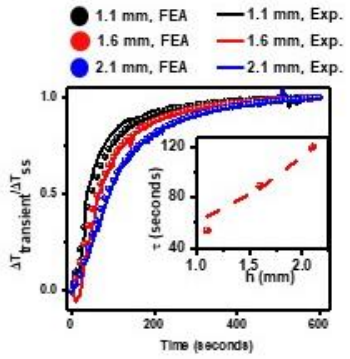

Fig. S9. Transient thermal analysis of flow. Experimental and simulated transient responses of $\Delta T_{sensors}/T_{actuator}$ for three different values of h_{skin} for Q_{flow} = 0.13 ml/min as a demonstration of an alternative method to quantify skin thickness, with data showing the relationship between the time constant (τ = time taken to reach 63.7% of steady-state value) and h_{skin} (inset), typically ~40s.

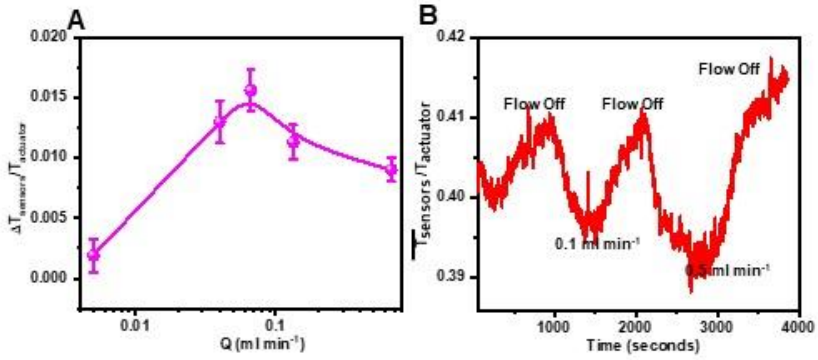

Fig. S10. Flow measurements through thick (6 mm) layers of soft tissue. (A) Steady-state in vitro experimental measurements of $\Delta T_{sensors}/T_{actuator}$ for a range of flow rates, for h_{skin} 6 mm, with error bars corresponding to standard deviations over an averaging window of 100s. **(B)** Time-dynamic in vitro experimental measurements of $\bar{T}_{sensors}/T_{actuator}$ for three flow rates (Q_{flow} = 0 ml/min, 0.1 ml/min, 0.5 ml/min), for h_{skin} = 6 mm.

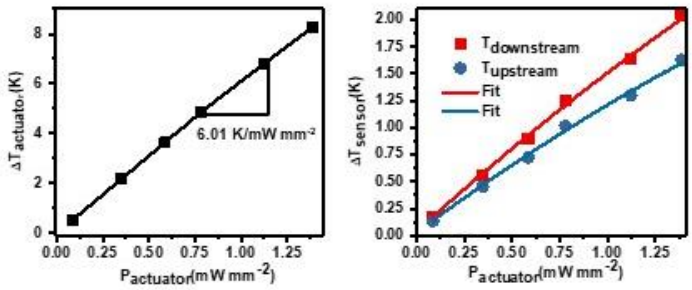

Fig. S11. Effect of actuator power. $T_{actuator}$ and $T_{sensors}$ as a function of power level for Q_{flow} = 0.13 ml/min on Sylgard 184 skin phantom, showing a linear relationship between the steady-state temperature attained by the actuator and supplied DC power (left), and increased value of ($T_{upstream}$-$T_{downstream}$) with increased actuator power (right). These trends translate into the increased SNR with power shown in Fig. 3G.

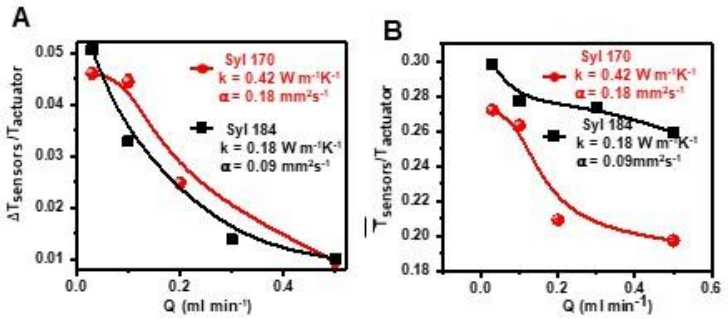

Fig. S12. Experimentally measured effects of changing skin thermal properties. ($\Delta T_{sensors}/T_{actuator}$) **(A)** and ($T_{downstream}+T_{upstream}$)/$2T_{actuator}$ **(B)** measured over skin phantoms with different thermal properties that bound naturally occurring variation in skin, $k_{sylgard\ 184}$ = 0.18 W $m^{-1}K^{-1}$,$\alpha_{sylgard\ 184}$=0.09 mm^2s^{-1} (black curves) and $k_{sylgard\ 170}$ = 0.42W $m^{-1}K^{-1}$, $\alpha_{sylgard\ 170}$ = 0.18 mm^2s^{-1} (red curves).

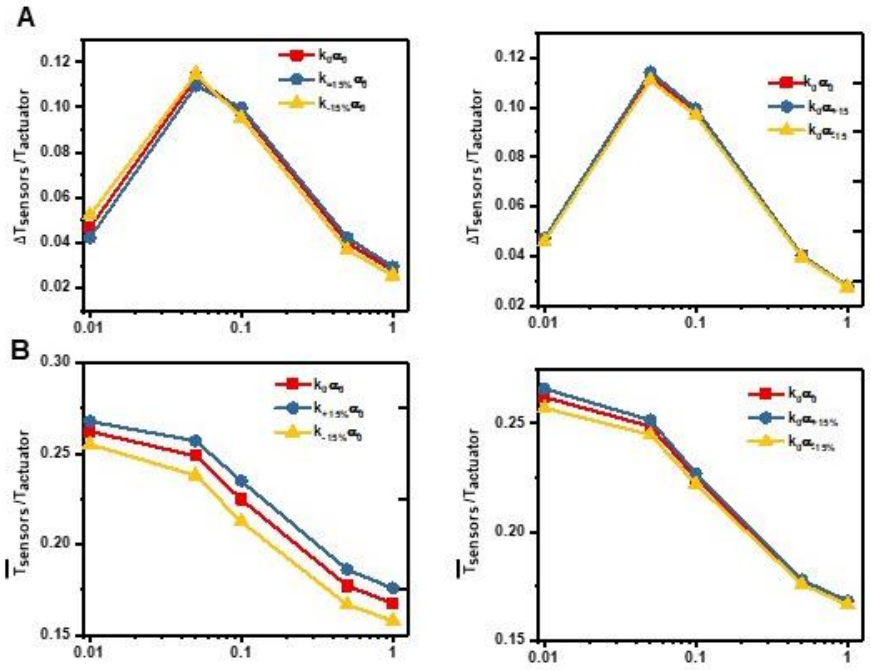

Fig. S13. Simulated effects of changing skin thermal properties. Effects of varying skin thermal properties k_{skin} and α_{skin} by $\mp$ 15% on **(A)** $\Delta T_{sensors}/ T_{actuator}$ and **(B)** $\bar{T}_{sensors}/T_{actuator}$, showing minimal change in $\Delta T_{sensors}/ T_{actuator}$ but a stronger effect on $\bar{T}_{sensors}/T_{actuator}$, as experimentally predicted

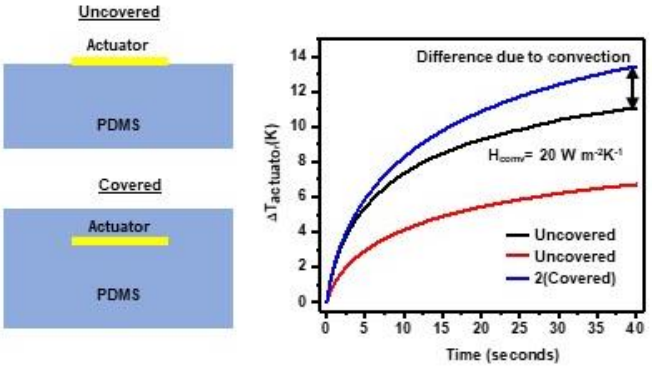

Fig. S14. Effect of ambient free air convection. Illustration of covered and uncovered actuator measurements (left) to yield transient rise curves, where the quantity $2(\Delta T_{covered})$-$T_{covered}$ can be curve-fitted to FEA models to yield the value of the convective heat transfer coefficient due to the free convection of air, here measured to be 20 W m^2K^{-1}, a value that is used for further FEA analysis.

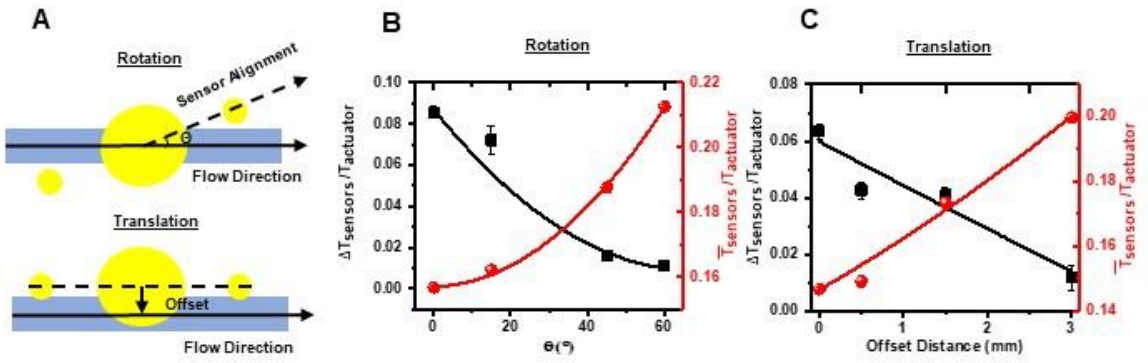

Fig. S15. Effect of uncertainty in placement. (A) Illustration and experimental data showing the effect of **(B)** rotational and **(C)** translational mispositioning on measured values of $\Delta T_{sensors}/T_{actuator}$ (black curve) and $\overline{T}_{sensors}/T_{actuator}$ (red curve).

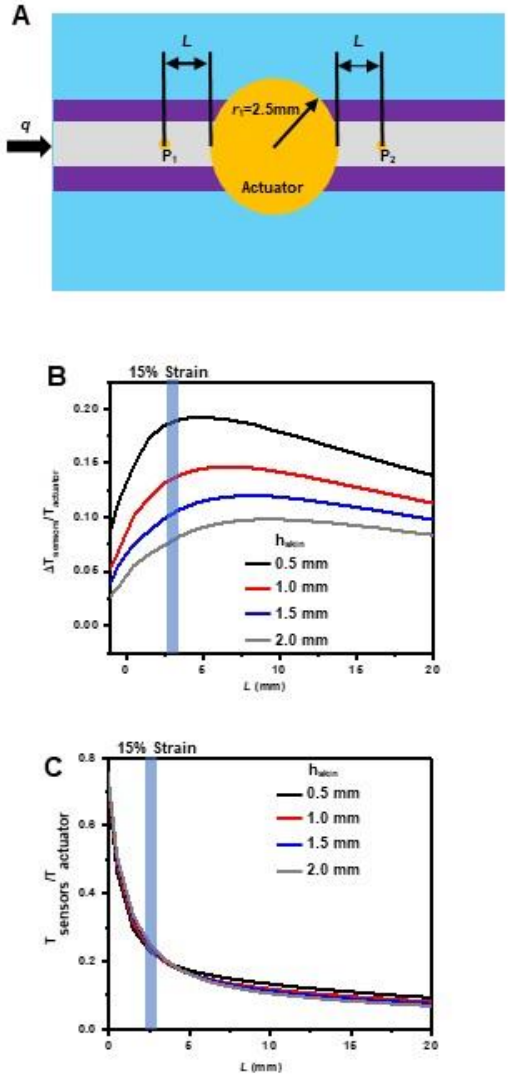

Fig. S16. Effect of altered intersensor distances. (A) Schematic illustration showing positions of actuator and upstream and downstream temperature sensors relative to underlying catheter. **(B)** FEA simulation of $\Delta T_{sensors}/T_{actuator}$ as a function of L, for h_{skin} = 0.5 mm, 1.0 mm, 1.5 mm, 2.0 mm, with the effect of 15% strain resulting in an altered inter-sensor positional uncertainty of ∓0.375 mm, as shown by the rectangular bar. **(C)** FEA simulation of $\bar{T}_{sensors}/T_{actuator}$ as a function of L, for h_{skin} = 0.5 mm, 1.0 mm, 1.5 mm, 2.0 mm, with the effect of 15% strain resulting in an altered inter-sensor positional uncertainty of ∓0.375 mm, as shown by the rectangular bar

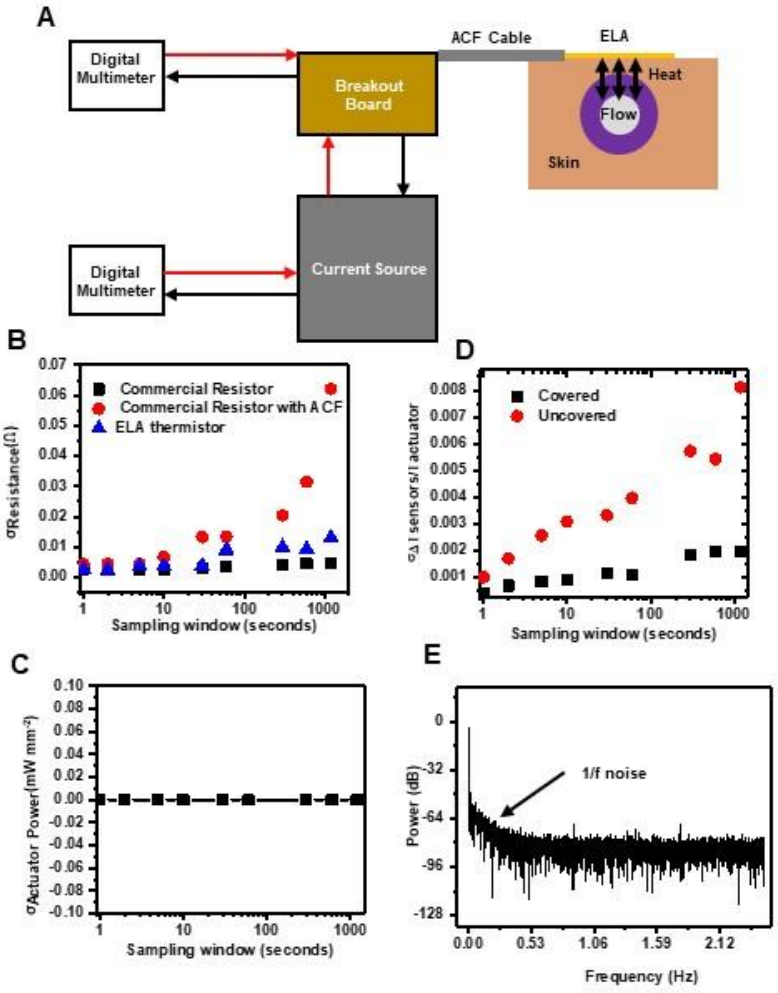

Fig. S17. Low-frequency dc noise sources. (A). Simplified schematic of the data acquisition system for the ELA. **(B)** Standard deviations as a function of sampling window for resistances measured by the ELA (black), a commercial sensor connected via ACF cable (blue) and a commercial resistor connected via soldered lead wires (red). **(C)** Standard deviation as a function of sampling window for actuator output power. **(D)** Standard deviation for measured $\Delta T_{sensors}/T_{actuator}$ as a function of sampling window for Q_{flow} = 0.13 ml min^{-1} on the benchtop system, when covered by an enclosure (black) and uncovered (red). **(E)** power spectral density for measured temperature at 5 Hz sampling rate over 1200 s.

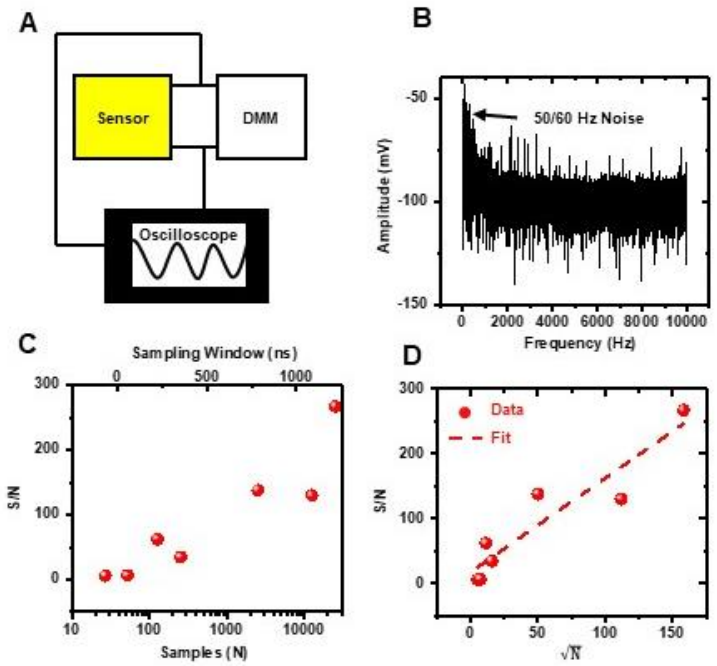

Fig. S18. High-frequency ac and dc noise. (A) Schematic illustration of the experimental system. **(B)** Fourier transform of resistance measured at 20 kHz. **(C)**. SNR, computed as the average of 5 successive resistance measurements divided by their standard deviation as a function of number of samples (N) and sampling window (time, ns). **(D)** Experimental data and linear fit for SNR as a function of $\sqrt{N}$.

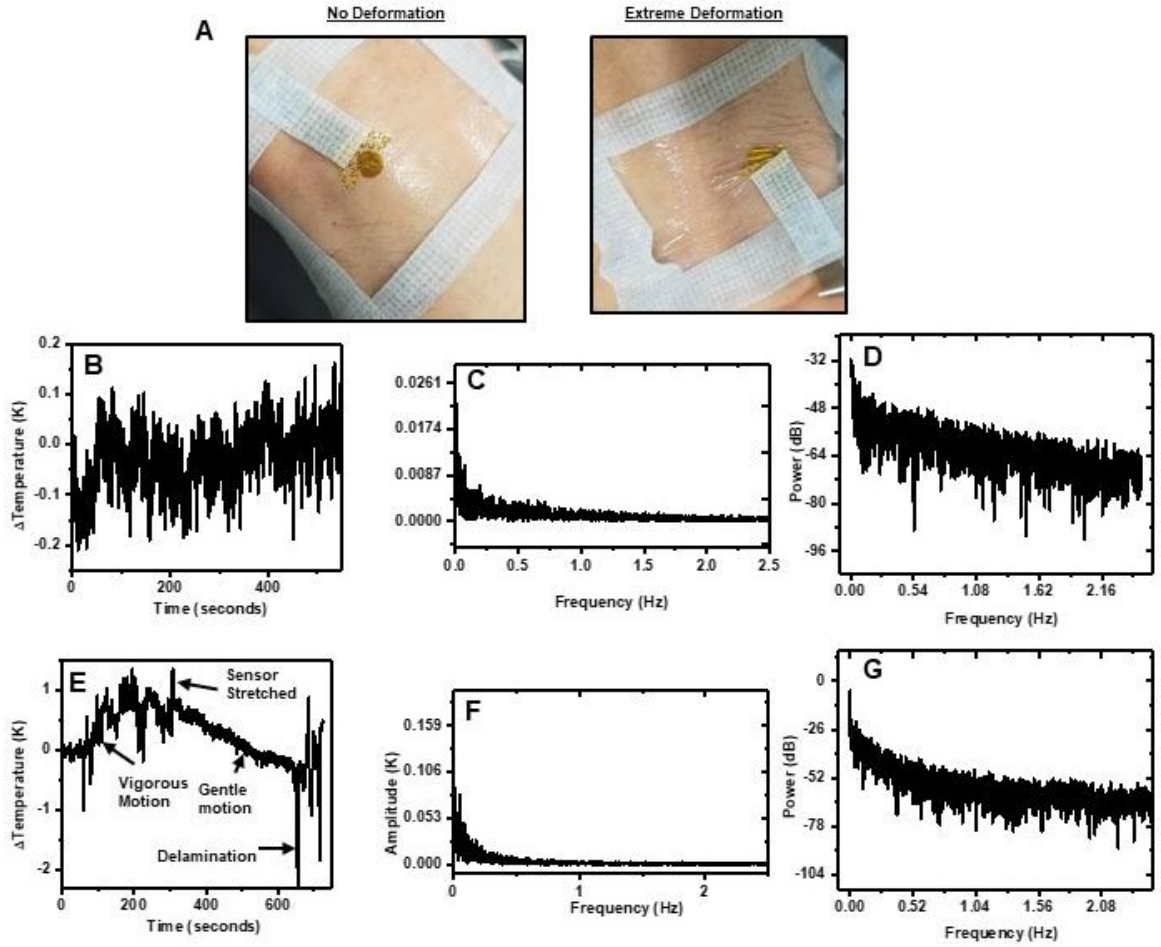

Fig. S19. In vivo noise. (A) Optical images illustrating no deformation (left) and extreme deformation (right) of sensor on skin. **(B-D)** Temperature fluctuations measured as a function of time (**B**), frequency (**C**) and as normalized power spectral density (**D**) on a stationary human subject. **E-G** Same as (B-D) on a vigorously moving subject.

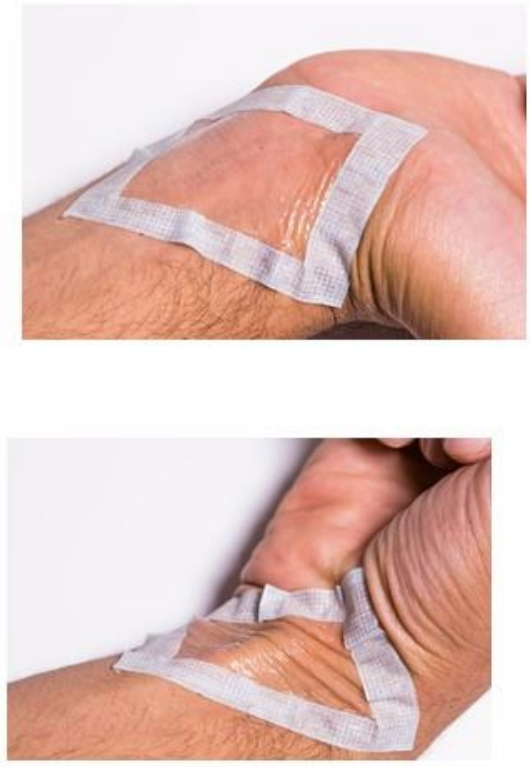

Fig. S20. Prevention of delamination during extreme deformation via adhesive design. Optical images of silicone adhesive, with E ~ 100 kPa and $q_{adhesion}$ = 160 N/m with tape frame, on the wrist of a human subject illustrating conformal contact during extreme deformation.

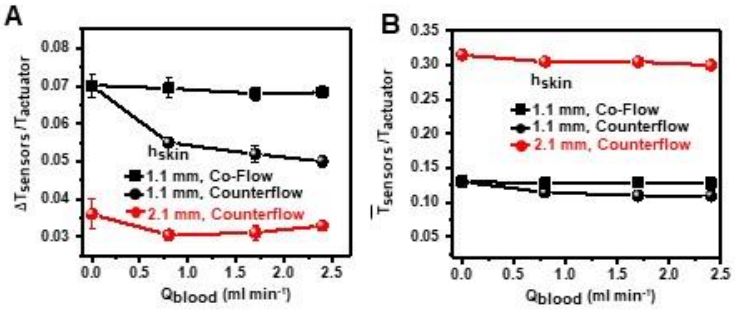

Fig. S21. Effect of near-surface blood vessels. ($\Delta T_{sensors}/T_{actuator}$) **(A)** and ($T_{downstream}+T_{upstream})/2T_{actuator}$ **(B)** measured in the presence of phantom blood flowing through adjacent tubes in co-flow (+x) and counter-flow (-x) configurations, for two values of h_{skin}, 1.1 mm (black curve) and 2.1 mm (blue curve)

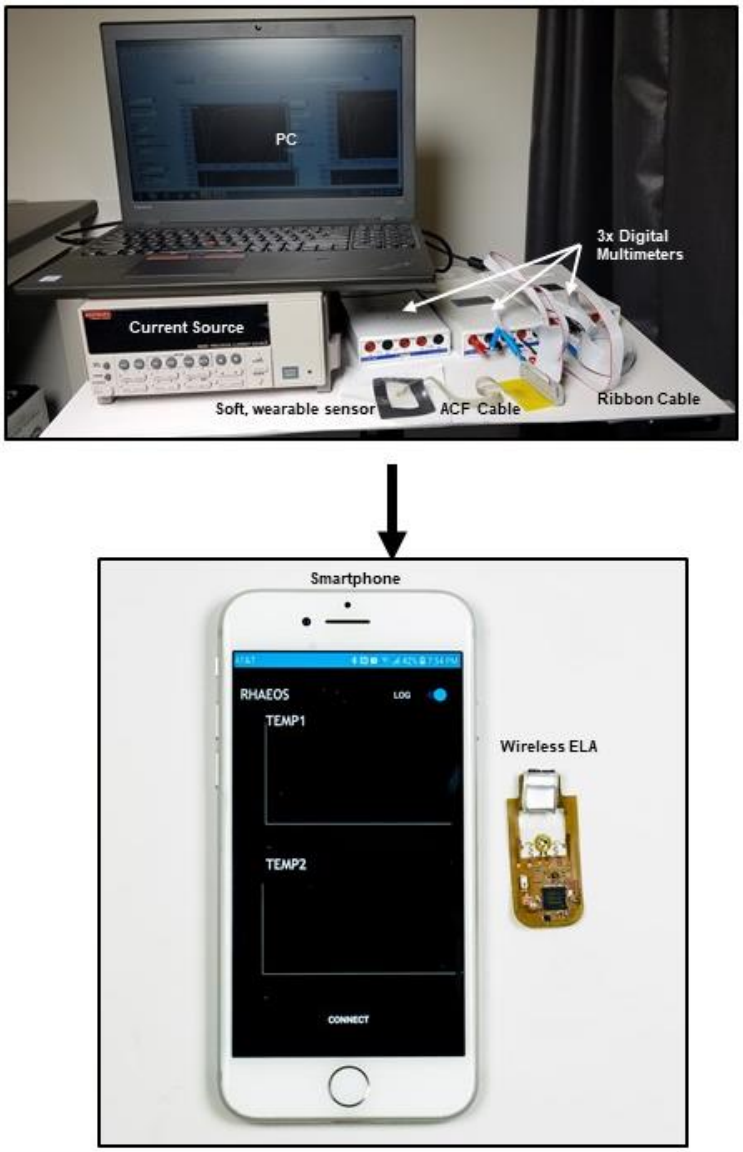

Fig. S22. Wired and wireless DAQ and control systems. Optical images of wired (top) and wireless (bottom) data acquisition systems, with accompanying sensors.

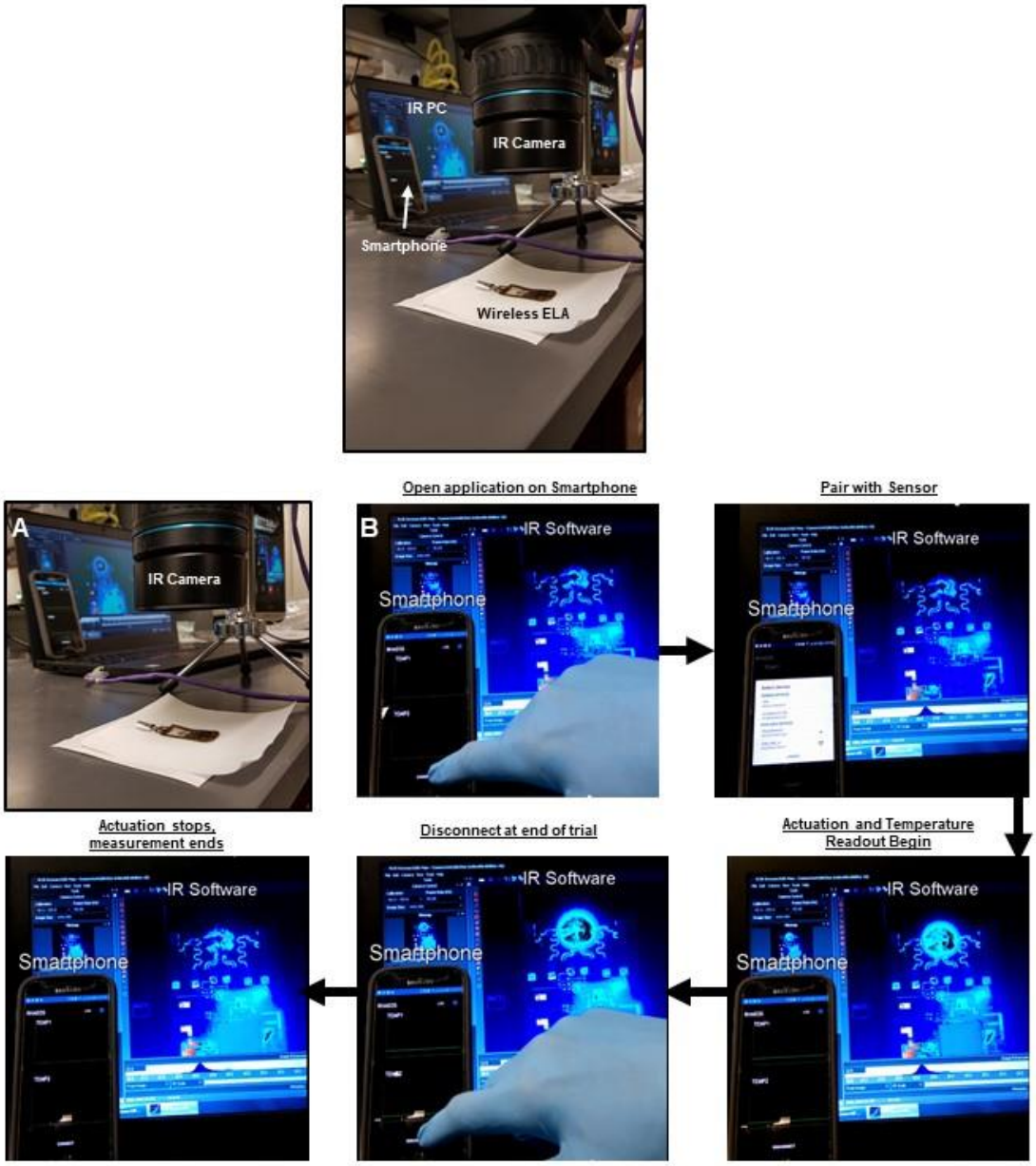

Fig. S23. Wireless control via smartphone. Series of images showing wireless embodiment under IR camera, with control smartphone and PC with IR-logging software in background, and wireless pairing and on-demand actuation using commercially available smartphone. These images are taken from, and are an accompaniment to, movies S1 and S2.

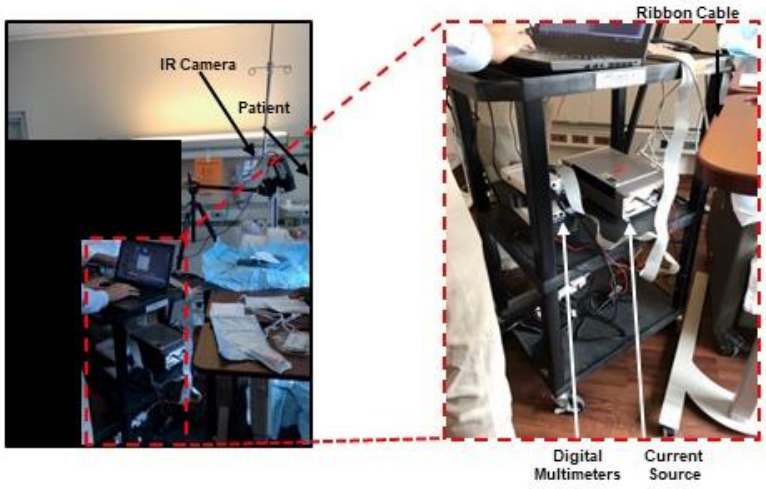

Fig. S24. Wired DAQ used in clinical trials. Images acquired inside patient room showing entire wired DAQ used for patient trials, along with IR camera.

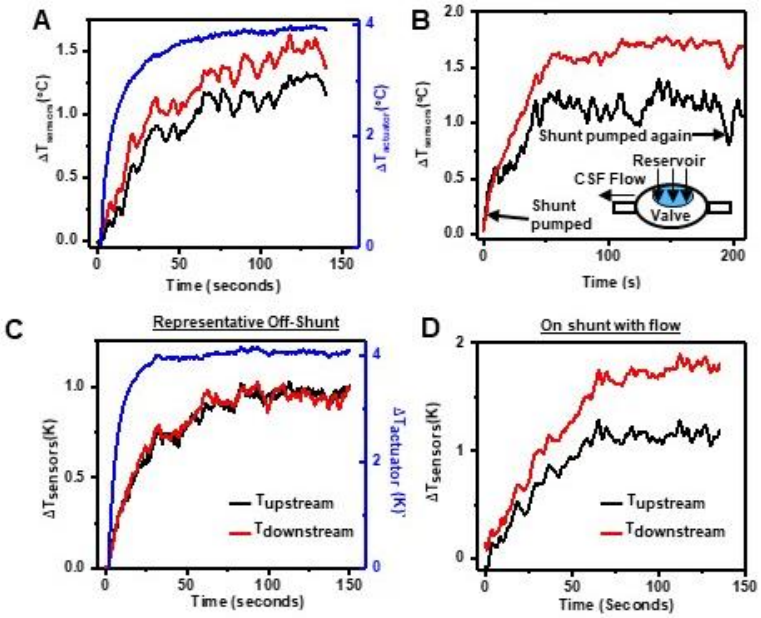

Fig. S25. Raw in vivo data. In-vivo $T_{actuator}$ (blue curve), $T_{uptream}$ (black curve) and $T_{downstream}$ (red curve) measurements as a function of time over on-shunt locations with (**A**) Low anisotropy, **(B-D)** clear high anisotropy and **(C)** no anisotropy

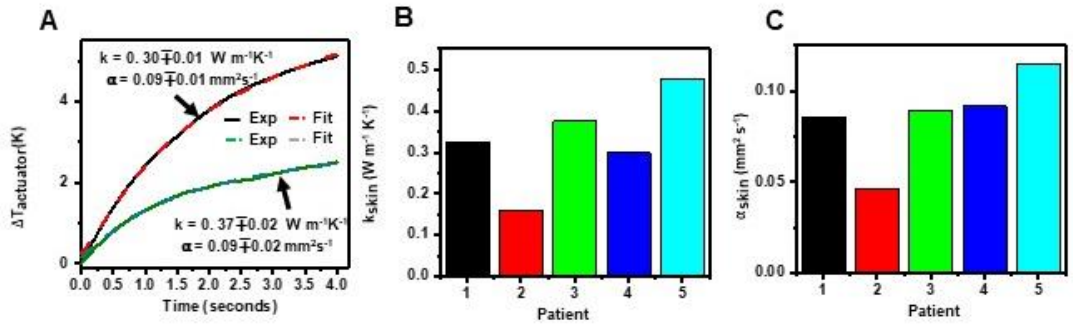

Fig. S26. In vivo measurements of skin thermal properties. (A) Representative transient measurement of $T_{actuator}$ for the off-shunt location, and transient plane source (TPS) curve fit to yield the thermal properties of the skin. (**B-C)** Computed values of (**B**) k_{skin} and (**C**) α_{skin} for each patient.

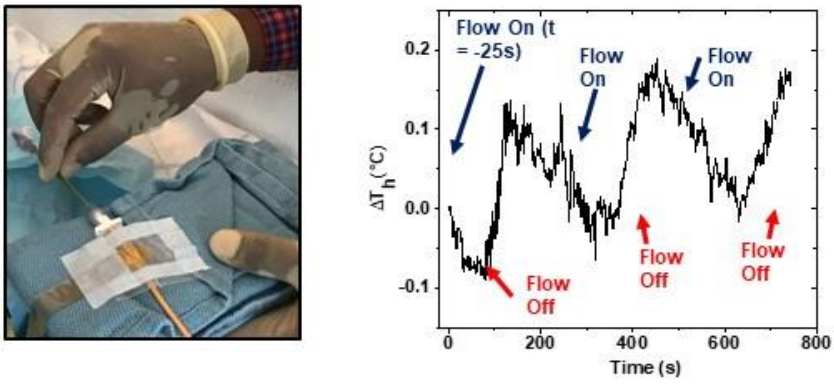

Fig. S27. Measurements made over EVD. (A) Image of ESA placed on external ventricular drain. **(B)** $T_{actuator}$ measurements on external ventricular drain as flow is varied by raising height of reservoir bag, thereby changing differential pressure.

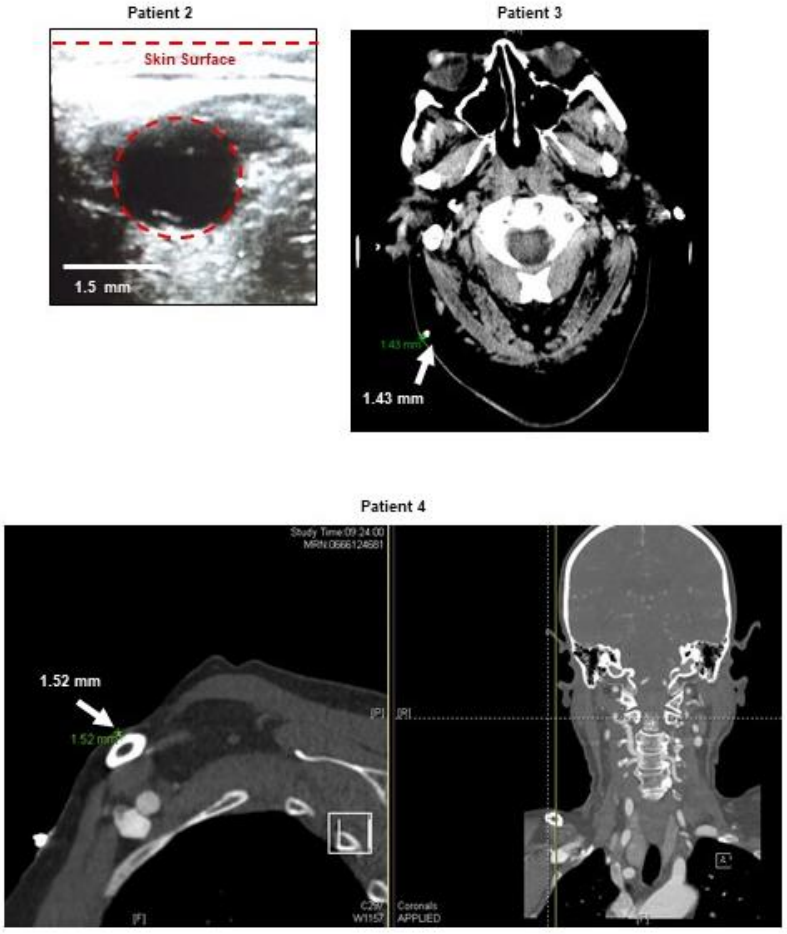

Fig. S28. In vivo measurements of skin thickness made via radiographic and ultrasound imaging. Ultrasound (patient 2) and CT (patients 3,4) images of patients over the location of device mounting, with accompanying skin thickness measurements, with the red dashed line indicating the outline of the shunt. Software-based measurements are available on CT images on patients 3 and 4, whereas the catheter (OD = 1.5 mm) serves as the scale bar for the Ultrasound image. The green text in the image is the same as the larger, white text, and indicates measured skin thickness.

Table S1. Thermal and geometrical quantities required for quantitative measurement of flow rate.

Quantity	Units	Range/Value	Measurement
k_{skin}	$W\ m^{-1}\ K$	0.30-0.50	In vivo with epidermal transient plane source
α_{skin}	$mm^2\ s^{-1}$	0.07-0.15	In vivo with epidermal transient plane source
$H_{convection}$	$W\ m^{-2}\ K$	6-25	In vitro, fitting to model
k_{CSF}	$W\ m^{-1}\ K$	0.5-0.6	Known *a priori*
α_{CSF}	$mm^2\ s^{-1}$	0.13-0.16	Known *a priori*
$k_{Catheter}$	$W\ m^{-1}\ K$	0.22	Known *a priori*
$\alpha_{Catheter}$	$mm^2\ s^{-1}$	0.12	Known *a priori*
h_{skin}	mm	1.5	Radiological and acoustic imaging, transient thermal measurements
$ID_{catheter}$	mm	1.0	Known *a priori*
$OD_{catheter}$	mm	1.5	Known *a priori*

Table S2. Summary of etiology of and measurements made on each patient.

	Underlying Condition	Age	Sex	Malfunction Present	Flow Detected (pre-intervention)	Flow Detected (post-intervention)	Imaging Correlate	Skin Irritation
1	Pseudotumor cerebri	36	F	Y	N	Y	Y[1]	N
2	Chiari I malformation	53	F	N	Y	N/A	N/A	N
3	Glioblastoma multiforme	32	M	N	Y	N/A	N/A	N
4	Glioblastoma multiforme	58	F	Y	N	Y	Y[2]	N
5	Post-hemorrhagic	30	F	Y	Y	N/A[3]	Y[4]	N

1. Patient had visualized kinking in the neck region on X-ray post initial surgery and clinically deteriorated the morning after initial shunt placement. Radionuclide shunt study showed aberrant distal flow.
2. Patient deteriorated post-surgery and was found to have severe stool burden on abdominal CT. After bowel regimen administered, patient clinically improved and sensor readings validated resolution of pseudoobstruction.
3. Device was inadvertently destroyed during final testing and postoperative readings were unable to be obtained. Patient was noted to have changes in flow pattern with inspiration and expiration corresponding to low drainage rate seen in OR due to concomitant distal and partial proximal obstructions.
4. CT scan demonstrated interval ventriculomegaly; radionuclide study demonstrated aberrant flow patterns; X-ray and abdominal CT demonstrated catheter malpositioned extraperitoneally near liver with adjacent fluid collection (likely CSF).

Table S3. Raw data measured on each patient.

Patient	$\Delta T_{sensors}/T_{actuator}$	σ	$\overline{T}_{sensors}/T_{actator}$	σ	Trial	Notes
1	0.0158243	0.005777	0.365	0.0106	On shunt	Pre-op, confirmed failure
1	0.028321	0.008057	0.222	0.0098	Off shunt	Pre-op, confirmed failure
1	0.2093394	0.021081	0.2916	0.0052	On shunt	Post-op, functioning shunt
1	0.0020478	0.042475	0.2612	0.0148	Off shunt	Post-op, functioning shunt
2	0.0084	0.0057	0.2676	0.0106	Off shunt	Functioning shunt
2	0.0518	0.0072	0.2289	0.011	On shunt	Functioning shunt
3	-0.0059732	0.001808	0.1601	0.003	Off shunt	Functioning shunt
3	0.0950298	0.003508	0.1815	0.0141	On shunt	Functioning shunt
4	-0.0061537	0.010499	0.2104	0.0079	Off shunt	Functioning shunt
4	0.0603105	0.00492	0.3	0.0058	On shunt	Functioning shunt
4	0.1009913	0.009832	0.2247	0.0086	On shunt	Functioning shunt, pumped
5	0.000963	0.033035	NA	NA	Off shunt	Malfunction with flow
5	0.1392	0.0146	0.3297	0.023	On shunt	Malfunction with flow

Table S4. Raw data and results from paired *t* tests for on-shunt and off-shunt measurements for patients with patent shunts.

Patient	$\Delta T_{sensors}/T_{actuator}$ On Shunt	$\Delta T_{sensors}/T_{actuator}$ Off Shunt
1	0.209339	0.00205
2	0.0518	0.0084
3	0.09503	-0.00597
4	0.100991	0.0061
5	0.1392	0.000963

Paired Samples Correlations

		N	Correlation	Sig.
Pair 1	OnShunt & OffShunt	5	.077	.901

Paired Samples Statistics

		Mean	N	Std. Deviation	Std. Error Mean
Pair 1	OnShunt	.11927	5	.059126	.026442
	OffShunt	.00258	5	.009056	.004050

Paired Samples Test

		Paired Differences			
					95% Confidence Interval of the Difference
		Mean	Std. Deviation	Std. Error Mean	Lower
Pair 1	OnShunt - OffShunt	.116688	.059118	.026438	.043283

Paired Samples Test

		Paired Differences			
		95% Confidence Interval of the Difference			
		Upper	t	df	Sig. (2-tailed)
Pair 1	OnShunt - OffShunt	.190093	4.414	4	.012

Table S5. Summary of technical challenges and key advancements over the course of patient study.

Problem	Discovery	Solutions
Skin adhesion	During initial patient trials, factors including cleanliness of skin, multiple device uses and patient movement resulted in the delamination of initial device iterations.	A device enclosure was constructed to work in tandem with a clinical grade, skin safe adhesive. The use of such adhesive prevented minor delamination and was viable for 10 attempted uses in a subsequent trial. The enclosure gave weight to the device and prevented errant movement with patient volatility, and delamination was minimized by sizing the enclosure to be larger than the area covered by the adhesive treated sensor.
Motion artifact	Normal and abnormal patient movement in an initial study resulted in aberrations in captured heat data.	AFC cables present a likely source of motion related noise. The wireless iteration of the device combined with subtraction algorithms and a narrowed accepted data range (given the obtained sample and future data) have and will continue to refine and eliminate this artifact.
Ease of handling	The initial trial saw a great deal of difficulty in device handling for the surgeon. Due to the adhesive involved, manipulation with gloved fingers was difficult. Excess traction put on the device and its elements led to poor performance both in terms of lamination and noise artifact engendered.	The device enclosure ideated resulted in a PDMS device frame designed to aid handling by the diagnostician. This not only reduced glove related device manipulation but facilitated swift application minimizing patient discomfort. Devices were more robust and performed admirably through periods of over 10 trials.
Alignment	Precise alignment of the sensor to the skin overlying tunnelled distal shunt catheter was occasionally difficult when attempting to approximate its center.	Winged attachments and central lines on the enclosure were designed on subsequent device iterations. These improved most applications from multiple attempts at placement to initial success in all subsequent trials. The winged attachments also had an unintended benefit to device handling.
Vasculature	Patients with prominent clavicular veins and superficial arterial branches adjacent to underlying shunt tubing were suspected of possible contamination.	Benchtop experiments simulated flow rates in shunts, venous and arterial sytems with varying flow experiments were conducted with a fluid injector into multiple caliber tubes.
Skin thickness	The depth of tunneled distal shunt catheters was suspected to differ among patients with varying habituses.	Benchtop experiments, radiographic data and the academic literature were consulted in the resolution of this important question. Anecdotally, over 10 surgeons stated that based on feel and experience alone, shunt catheters were likely 1-8 mm under the skin. Further experiments demonstrated sensor performance to a depth of 6 mm. Measurements shunt catheter to surface distance of available computerized tomography scans of patients was also performed, with an average total thickness of subcutaneous tissue overlying the distal catheter of 1.52 mm. Finally, a comprehensive literature search was performed. Established factors including total soft tissue to bony protuberance distance to skin (under 2 mm),

Table S6. Summary of existing shunt diagnostic tools.

Modality	Cost	Time (min)	Sensitivity	Specificity	PPV	NPV
X-Ray	**440**	**84**	**4-26%**	**92-99%**	**13**	**93.9**
CT	**1323**	**83**	**54-80%**	**80-90%**	**71**	**90.8**
MRI	**3239**	**115**	**40-62.8%**	**84-92%**	**75**	**86.5**
RSPS	**750**	**45**	**47-65%**	**86-92%**	**71**	**71**
ShuntCheck	**Unknown**	**6**	**80%**	**100%**	**58**	**96**